minerals

Article

Early Permian Post-Collision Extensional Setting in the Southern Beishan Orogenic Belt: Evidence from the Zhangfangshan Granodiorite and the Baishantang Bimodal Volcanic Rocks

Lei Wu [1], Xinwei Zhai [1,*], Erteng Wang [1], Wanfeng Chen [2], Gaorui Song [1], Feifei Zheng [1], Jiaolong Zhao [1], Jinrong Wang [1] and Haidong Wang [1]

[1] Key Laboratory of Mineral Resources in Western China (Gansu Province), School of Earth Sciences, Lanzhou University, Lanzhou 730000, China; wul20@lzu.edu.cn (L.W.); wanget19@lzu.edu.cn (E.W.); songgr21@lzu.edu.cn (G.S.); zhengff2023@lzu.edu.cn (F.Z.); jlz@lzu.edu.cn (J.Z.); jrwang@lzu.edu.cn (J.W.); whaidong2023@lzu.edu.cn (H.W.)

[2] College of Geography and Tourism, Hunan University of Arts and Science, Changde 430700, China; epwanfeng@163.com

* Correspondence: zhaixw926@lzu.edu.cn

Abstract: Outcrops of late Paleozoic magmatic rocks are common in the Southern Beishan Orogenic Belt (SBOB), Southern Central Asian Orogenic Belt (CAOB), which is a key object for the understanding of regional tectonism and defining the final closure time of the Paleo-Asian Ocean (PAO). We present zircon U-Pb chronology and whole-rock geochemistry data for late Paleozoic granodiorites and bimodal volcanic rocks from the Shuangyingshan-Huaniushan unit in the north Huitongshan-Zhangfangshan ophiolitic belt in the SBOB. The Zhangfangshan granodiorites (LA-ICP-MS, Ca. 288 Ma) are A2-type granite enriched in Rb, Th, Pb and LREEs and depleted in Nb, Ta, Ti, Sr, Ba and HREEs. They have varying MgO and $^{T}Fe_2O_3$ contents with high $Mg^{\#}$ (38.56~48.97) values; the Lu/Yb ratios (0.14~0.15) of these granodiorites are similar to mantle-derived magma. A clear plagioclase zoning structure and acicular apatite occur in mineral assemblages derived from magma mixing between mafic and felsic magmas. The Baishantang bimodal volcanic rocks (272 Ma) consist of rhyolite and basaltic andesite. Baishantang rhyolites are A2-type felsic rock enriched in Rb, Th, Pb and LREEs and depleted in Nb, Ta, Ti, Sr, Ba and HREEs, with negative $\varepsilon_{Nd}(t)$ and $\varepsilon_{Hf}(t)$ (−5.2~−4.8 and −2.2~−1.9, respectively). Rhyolites originated from the partial melting of the crust, influenced by mantle material. Basaltic andesites belong to calc-alkaline series and have an enrichment of Rb, Ba, Th, U, Pb and LREEs, are weakly enriched in Zr-Hf, and are depleted in Nb, Ta, Ti and HREEs. The Nd-Hf isotopes of these basaltic andesites are not coupled with negative $\varepsilon_{Nd}(t)$ (−2.8~−0.4) and positive $\varepsilon_{Hf}(t)$ (1.8~5.5) values. These characteristics indicate that they originated from the partial melting of the mantle mixed with sediment-derived melts. In combination with previous studies, our findings show that the early Permian Zhangfangshan granodiorites and Baishantang bimodal volcanic rocks formed in a post-collision extensional setting, and the Huitongshan-Zhangfangshan ocean had been closed before early Permian.

Keywords: early Permian; post-collisional extension environment; granodiorite; bimodal volcanic rocks; Beishan Orogenic Belt

check for updates

Citation: Wu, L.; Zhai, X.; Wang, E.; Chen, W.; Song, G.; Zheng, F.; Zhao, J.; Wang, J.; Wang, H. Early Permian Post-Collision Extensional Setting in the Southern Beishan Orogenic Belt: Evidence from the Zhangfangshan Granodiorite and the Baishantang Bimodal Volcanic Rocks. *Minerals* **2023**, *13*, 1468. https://doi.org/10.3390/min13121468

Academic Editors: Alexey V. Ivanov, Jiafu Chen, Nan Ju and Zhonghai Zhao

Received: 2 October 2023
Revised: 14 November 2023
Accepted: 16 November 2023
Published: 22 November 2023

1. Introduction

The Central Asian Orogenic Belt (CAOB), is the largest Phanerozoic accretionary orogenic belt in the world, situated between the European, Sibrian, Tarim and North China cratons (Figure 1a) [1–5]. The CAOB evolved from the Neoproterozoic to the late Paleozoic–early Mesozoic through multiple accretion of arc/back-arc systems, ophiolites and microcontinental fragments during the closure of the Paleo-Asian Ocean (PAO) [5–8].

Voluminous magmatic and metamorphic rocks are widely exposed in CAOB and associated with accretionary, intra-continental, collisional and post-collisional processes [9–14], and the reference therein. These magmatic and metamorphic rocks provide good clues for the study of the closure time of PAO and evolution process of orogenic belt.

The Beishan Orogenic Belt (BOB), located in the southern margin of the CAOB, is an important part of the CAOB (Figure 1). It is a key area in the study of the tectonic evolution of the southern CAOB and the closure time of the PAO [15]. Four magmatic events occurred in the BOB [16]: Mesoproterozoic magmatic events representing the formation of an ancient basement in the Southern Beishan Orogenic Belt (SBOB) [17,18]; Neoproterozoic magmatism which represents the reworked ancient crust during the evolution of the Rodinia supercontinent [19,20]; Cambrian-Silurian arc magmatism related to the subduction of the Beishan ocean/PAO [21–23]; Ordovician–early late Paleozoic magmatic events correlating with the opening and closure of the branch of PAO [16,24], and the reference therein. Although a large number of late Paleozoic igneous rocks are distributed in the SBOB (Figure 1b), the formation environment of these magmatic rocks is still controversial (subduction, syn-collision or post collision) [12–14,25–30], which hampers the understanding of the final closure time of the PAO [12–14,25–30] and the tectonic evolution of the SBOB. The study of Carboniferous-Permian magmatism, especially magmatic rocks intruded into the ophiolites, provides an ideal target to investigate the late Paleozoic tectonic evolution of the SBOB and the final closure time of the PAO.

In this paper, we focus on the early Permian Zhangfangshan granodiorite intruded into the Zhangfangshan ophiolites and Baishantang bimodal volcanic rocks in the SBOB (Figure 1b) using zircon U-Pb isotopic dating, whole-rock major oxides, trace elements and Nd-Hf isotopic analysis in order to discuss their petrogenesis and the implications for the closure time of PAO and the tectonic evolution of the SBOB.

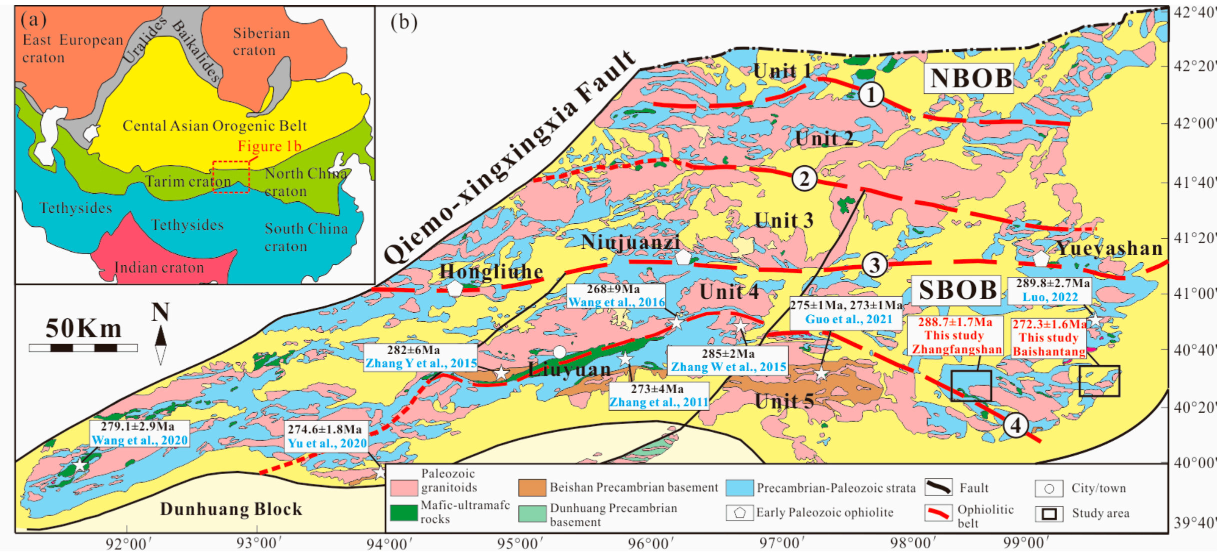

Figure 1. (**a**) Simplified tectonic map of the Central Asian Orogenic Belt showing the location of the Beishan Orogenic Belt (BOB) (modified after [31]). (**b**) Simplified geological map of the BOB (modified after [17]). (**b**) Early Permian magmatism in the SBOB (age data are taken from [13,26,32–37]). (1): Hongshishan ophiolitic belt; (2): Jijitaizi-Xiaohuangshan ophiolitic belt; (3): Hongliuhe-Niujuanzi-Yueyashan ophiolitic belt; (4): Huitongshan-Zhangfangshan ophiolitic belt; Unit 1: Queershan unit; Unit 2: Heiyingshan-Hanshan unit; Unit 3: Mazongshan unit; Unit 4: Shuangyingshan-Huaniushan unit; Unit 5: Shibanshan unit.

2. Geological Setting

The BOB is located at the southern margin of the CAOB and juxtaposed against the Dunhuang block to the south [15,17,30]. From north to south, there are four important ophiolite belts in the BOB, namely, Hongshishan, Jijitaizi-Xiaohuangshan, Hongliuhe-Niujuanzi-Yueyashan (HNY) and Huitongshan-Zhangfangshan (HZ) ophiolitic belts (Figure 1b) [30,38–41]. The BOB is sub-divided into Queershan, Heiyingshan-Hanshan, Mazongshan, Shuangyingshan-Huaniushan (SH) and Shibanshan units from north to south by these ophiolitic belts (Figure 1b) [15].

The study regions are located at the SH unit bounded by the HNY ophiolitic belt to the north and the HZ ophiolitic belt to the south. Neoproterozoic–late Paleozoic strata and intrusive rocks are widely exposed in this unit. Neoproterozoic-Cambrian strata are mainly composed of metasedimentary-sedimentary rocks [42]. Ordovician-Devonian strata are characterized by volcano-sedimentary formations. Carboniferous clastic and carbonate strata are sparsely distributed in this unit. Permian clastic and volcanic rocks are mainly exposed on the southern margin of the SH unit [43,44].

The Zhangfangshan granodiorite and the Baishantang bimodal volcanic rocks crop out in the east of the SH unit. The Zhangfangshan granodiorite is located in the north of the Zhangfangshan ophiolitic belt and west of the Baishantang area, intruded into the Ordovician-Silurian strata, ophiolites and Carboniferous strata while making unconformable contact with Jurassic strata (Figures 2a and 3a,b).

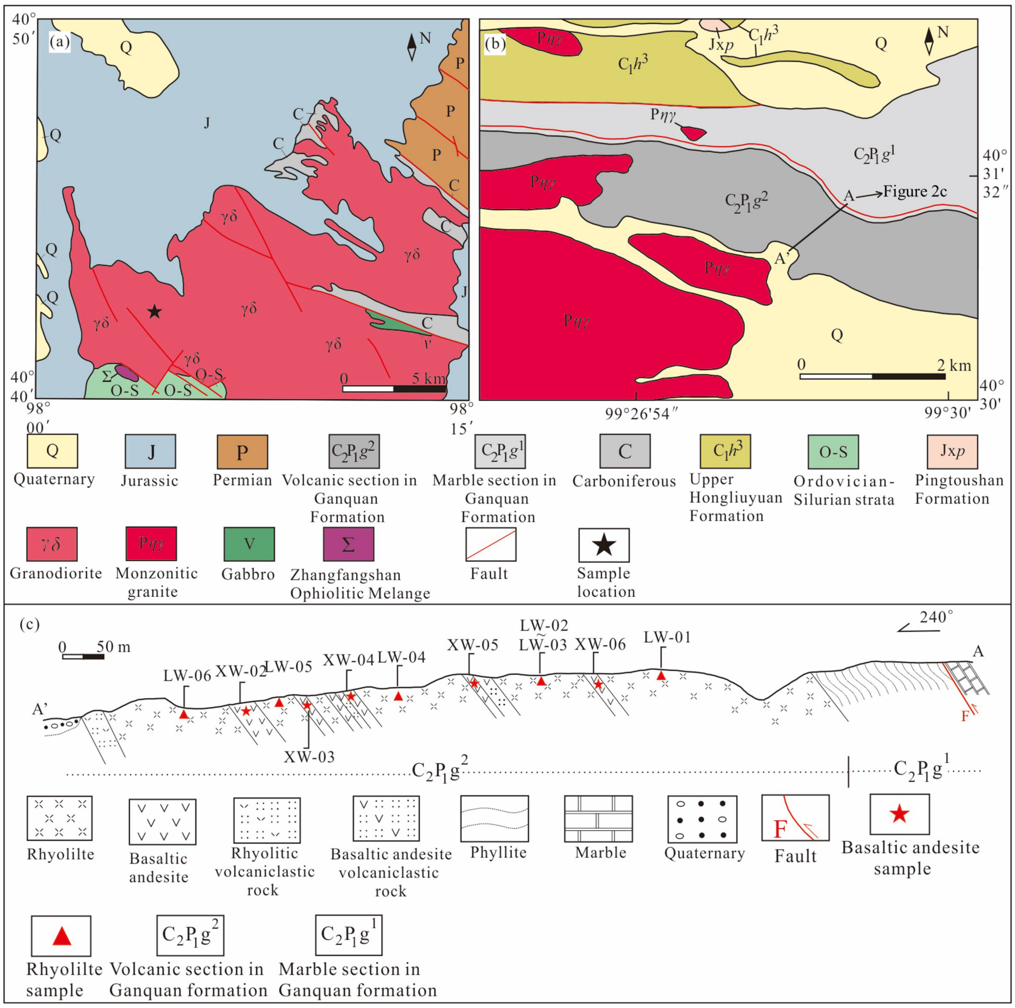

Figure 2. Geological maps of (**a**) the Zhangfangshan granodiorite and (**b**) the Baishantang bimodal volcanic rocks (after [45,46]); (**c**) profile of the Baishantang bimodal volcanic rocks.

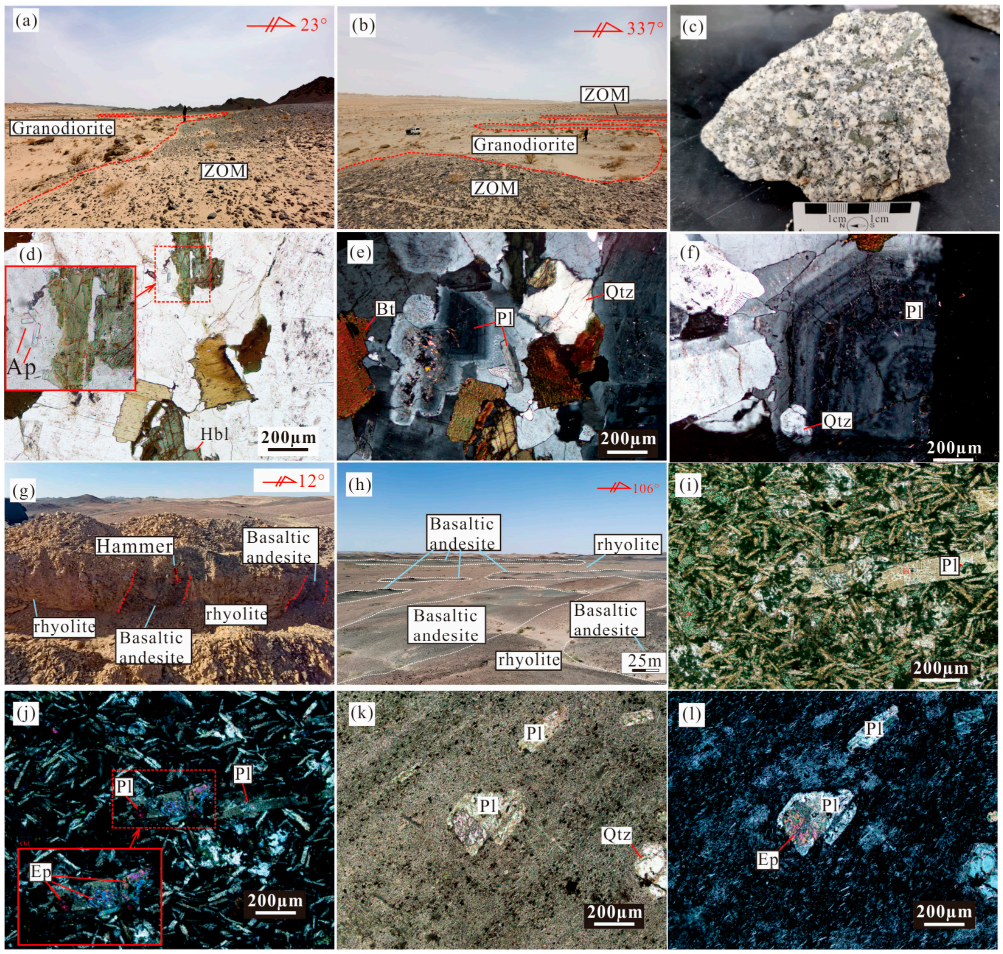

Figure 3. Field photos and photomicrographs of the Zhangfangshan granodiorite and Baishantang bimodal volcanic rocks. (**a**,**b**) Zhangfangshan granodiorite intruded into Zhangfangshan ophiolitic mélange (ZOM); (**c**) Photo of the Zhangfangshan granodiorite sample. Hornblende can be clearly seen in the rock; (**d**–**f**) Photomicrographs of the Zhangfangshan granodiorite. Tiny acicular apartite and zonal structure of plagioclase are detected (**d**,**f**). The mineral assemblages of granodiorite (**e**). Quartz crystal as inclusions occur in plagioclase (**f**); (**g**,**h**) Field photos of the Baishantang bimodal volcanic rocks. Rhyolite and basaltic andesite are interbedded (**g**), and the distribution area of rhyolite is larger than that of basaltic andesite (**h**); (**i**) Plane-polarized photograph of basaltic andesite; (**j**) Cross-polarized photograph of basaltic andesite, where epidotization occurs in plagioclase; (**k**) Plane-polarized photograph of rhyolite; (**l**) Cross-polarized photograph of rhyolite, where epidotization occurs in plagioclase. Ap: apatite; Hbl: hornblende; Bt: biotite; Pl: plagioclase; Qtz: quartz; Chl: chlorite; Ep: Epidote.

The Baishantang bimodal volcanic rocks are exposed in the volcanic section in Ganquan Formation. The Ganquan Formation is exposed in the south of the Hongliuyuan Formation and separated from it by faults (Figure 2b). The Ganquan Formation can be divided into marble and volcanic sections. The marble section is mainly composed of marble with rhyolite, phyllite, mica quartz schist and metabasaltic and is separated from the volcanic section by a fault to the south. The volcanic section is mainly composed of rhyolite and basaltic andesite, with a small amount of rhyolitic and basaltic andesite pyroclastic rocks. Rhyolites have larger distribution areas than the basaltic andesites, and they are interbedded to form bimodal volcanic rocks (Figures 2c and 3g,h). Due to intense weathering, only few complete rhyolite and basaltic andesite outcrops can be seen in the study area.

3. Sample Description

3.1. Zhangfangshan Granodiorite

The granodiorite is grayish white, medium- to coarse-grained and massive structure. Its mineral composition includes plagioclase (40~45 vol%), quartz (35~40 vol%), biotite (10~15 vol%) and hornblende (5~10 vol%). Accessory minerals include apatite, zircon and others (Figure 3d–f). One sample was collected for zircon U-Pb dating, and six samples were collected for the whole-rock major oxides and trace elements study.

3.2. Baishantang Bimodal Volcanic Rocks

The rhyolite is light red to light pink in color, massive and porphyritic in texture, with up to 20 vol% phenocrysts, mainly comprising plagioclase and a minor amount of quartz (Figure 3k,l). The directional arrangement of phenocrysts can be observed in Figure 3k,l. The groundmass is usually a fine-grained assemblage of feldspar, quartz and minor Fe-Ti oxides. Plagioclase has a certain degree of kaolinization and epidotization.

The basaltic andesite is dark grey with a typical porphyritic texture (Figure 3i,j). The phenocrysts are mainly plagioclase (~15 vol%), while the matrix consists of plagioclase microcrystals and accessory minerals. Plagioclase has a certain degree of kaolinization and epidotization. One rhyolite was collected for zircon U-Pb dating; six rhyolite samples and five basaltic andesite samples were collected for whole-rock major oxides and trace elements study. Three rhyolite samples and three basaltic andesite samples were collected for the whole rock Nd-Hf isotopes analysis.

4. Analytical Methods

4.1. Zircon U-Pb Dating

Zircon cathodoluminescence (CL) images of the Zhangfangshan granodiorite and the Baishantang rhyolite were taken at the Key Laboratory of Mineral Resources of Western China, Lanzhou University, Lanzhou, China, and Langfang Chenxin Geological Service Co., Hebei, China, respectively. After separation using the conventional heavy liquid and magnetic techniques, zircon grains were purified through hand-picking under a binocular microscope, embedded in an epoxy and then polished to expose half of the zircon grains [47]. The zircon grains with internal ring structures, no clear inclusions and few fractures in the CL were chosen for U-Pb dating. Zircon LA-ICP-MS U-Pb isotope analyses were performed at the Key Laboratory of Mineral Resources of Western China, Lanzhou University, using ICP-MS Agilent 7500a (Agilent, Santa Clara, CA, USA). The zircon standard 91500 [48] was used as the age reference. The glass NIST 610 and Si were used as an internal standard for Pb, Th and U [49]. The Glitter (ver. 4.0) [50] and Isoplot R [51] programs were employed to process the data. The analytical procedures are described in detail by Yuan et al. [52].

4.2. Whole-Rock Major Oxides and Trace Elements Analyses

All analyses of major oxides and trace elements for the Zhangfangshan granodiorite and Baishantang bimodal volcanic rocks were carried out at the Key Laboratory of Mineral Resources of Western China, Lanzhou University. Major oxides were determined through ICP optical emission spectroscopy (ICP-OES) (manufactured by Agilent, Santa Clara, CA, USA) using a Leeman Prodigy system with analytical precision greater than 2%. Loss on ignition (LOI) was obtained by heating approximately 0.5 g of the dried-sample powder at 1000 °C for 2 h. Trace elements were determined through inductively coupled plasma mass spectrometry (ICP-MS) using an Agilent 7700× system. The relative standard deviation was less than 10% for the determination of trace elements, including rare earth elements (REEs). The US Geological Survey reference materials AGV-2 and BCR-2 were used as standards. Analytical procedures of major oxides and trace elements have been described by Li et al. [53] and Gao et al. [54], respectively.

4.3. Whole-Rock Nd-Hf Isotope Analyses

Sm-Nd and Lu-Hf isotopic analyses were performed on Nu Instruments Nu Plasma II MC-ICP-MS (Nu Instrument, Wrexham, Wales, UK) at the Key Laboratory of Mineral Resources of Western China, Lanzhou University. The US Geological Survey reference materials BCR-2 and AGV-2 were used as standards. JNDI and Alfa Hf standard solution were periodically analyzed to correct instrumental drift. Mass fractionation corrections for Nd and Hf isotopic ratios were based on 0.7219 for $^{146}Nd/^{144}Nd$ and 0.7325 for $^{179}Hf/^{177}Hf$, respectively. Standard BCR-2 yielded average values of 0.512642 ± 0.00003 (2σ, n = 5) for $^{143}Nd/^{144}Nd$ and 0.282871 ± 0.00004 (2σ, n = 2) for $^{176}Hf/^{177}Hf$. Standard AGV-2 yielded 0.512742 ± 0.00003 (2σ, n = 5) for $^{143}Nd/^{144}Nd$ and 0.282950 ± 0.00004 (2σ, n = 1) for $^{176}Hf/^{177}Hf$. Analytical procedures were described by Bao et al. [55].

5. Analytical Results

The zircon U-Pb isotopic data, whole-rock major oxides, trace element data and Nd-Hf isotopic data are listed in Supplementary Table S1, Table S2 and Table S3, respectively.

5.1. Zircon U-Pb Geochronology

Fifteen zircons from the granodiorite samples are euhedral to subhedral and columnar in shape, with length-to-width ratios of 2:1~3:1. The zircons display well-preserved concentric oscillatory zoning (Figure 4a) and high Th/U ratios (0.44~0.65) (Table S1), indicating a typical magmatic origin [56]. All fifteen analyses yielded similar apparent $^{206}Pb/^{238}U$ ages of 297~284 Ma, with a weighted mean age of 288.7 ± 1.7 Ma (MSWD = 1.1, n = 15) (Figure 5a).

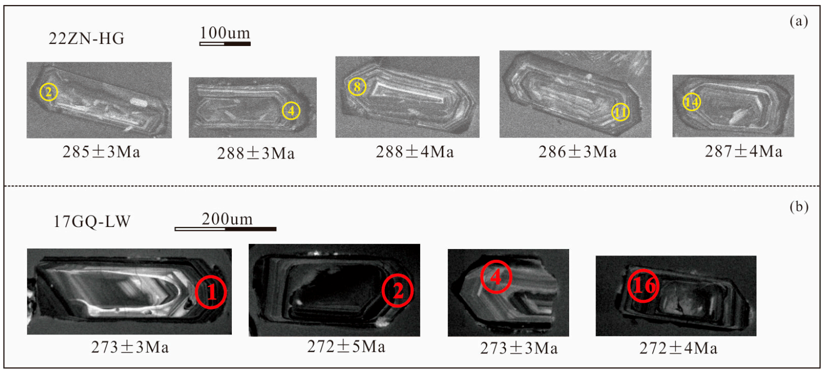

Figure 4. Representative zircons cathodoluminescence images for zircons in the Zhangfangshan granodiorite (**a**) and the Baishantang rhyolite (**b**). Yellow and red numbers represent the U-Pb analytical sites of the Zhangfangshan granodiorite and the Baishantang rhyolite, respectively.

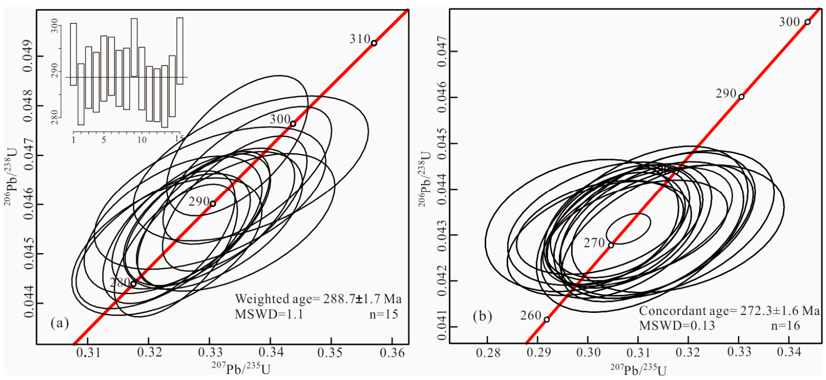

Figure 5. U-Pb dating results of zircons for the Zhangfangshan granodiorite (**a**) and the Baishantang rhyolilte (**b**).

Eighteen zircons from the Baishantang rhyolite are euhedral to subhedral and display well-preserved concentric oscillatory zoning (Figure 4b). Their Th/U ratios are 0.46~1.30 (Table S1), indicating a typical magmatic origin. Sixteen analyses yield close apparent $^{206}Pb/^{238}U$ ages of 271~273 Ma and a concordant age of 272.3 ± 1.6 Ma (MSWD = 0.13, n = 16) (Figure 5b). The other two analyses yield old $^{206}Pb/^{238}U$ ages (both of GQ-LW-03 and GQ-LW-07 are 395 Ma) (Table S1).

5.2. Whole-Rock Major Oxides and Trace Elements

5.2.1. The Zhangfangshan Granodiorite

The composition of major oxides is as follows: SiO_2 (64.78~69.21 wt.%), Al_2O_3 (13.55~14.58 wt.%), $^TFe_2O_3$ (2.04~3.47 wt.%), MgO (0.65~1.68 wt.%), Na_2O (3.92~7.22 wt.%), K_2O (3.20~4.03 wt.%) and TiO_2 (0.33~0.40 wt.%). The $Na_2O + K_2O$ values are 7.12~10.74 wt.%, $Mg^{\#}$ values are 38.56~48.97 and A/CNK ratios are less than 1 (0.62~0.90). The samples' plots are in the granite field and are high-K calc-alkaline series and metaluminous (Figure 6). Chondrite-normalized REE patterns of Zhangfangshan granodiorites (Figure 7a) show a weakly fractionated REE pattern ($(La/Yb)_N$ = 3.39~5.27), enrichments of LREEs (LREE/HREE = 4.08~6.14) and negative Eu anomalies (δEu = 0.27~0.48). Primitive mantle-normalized trace elements' patterns (Figure 7b) show enrichments of Rb, Th and Pb; weak enrichments of Zr and Hf; and a depletion of Nb, Ta, Ti, Sr and Ba.

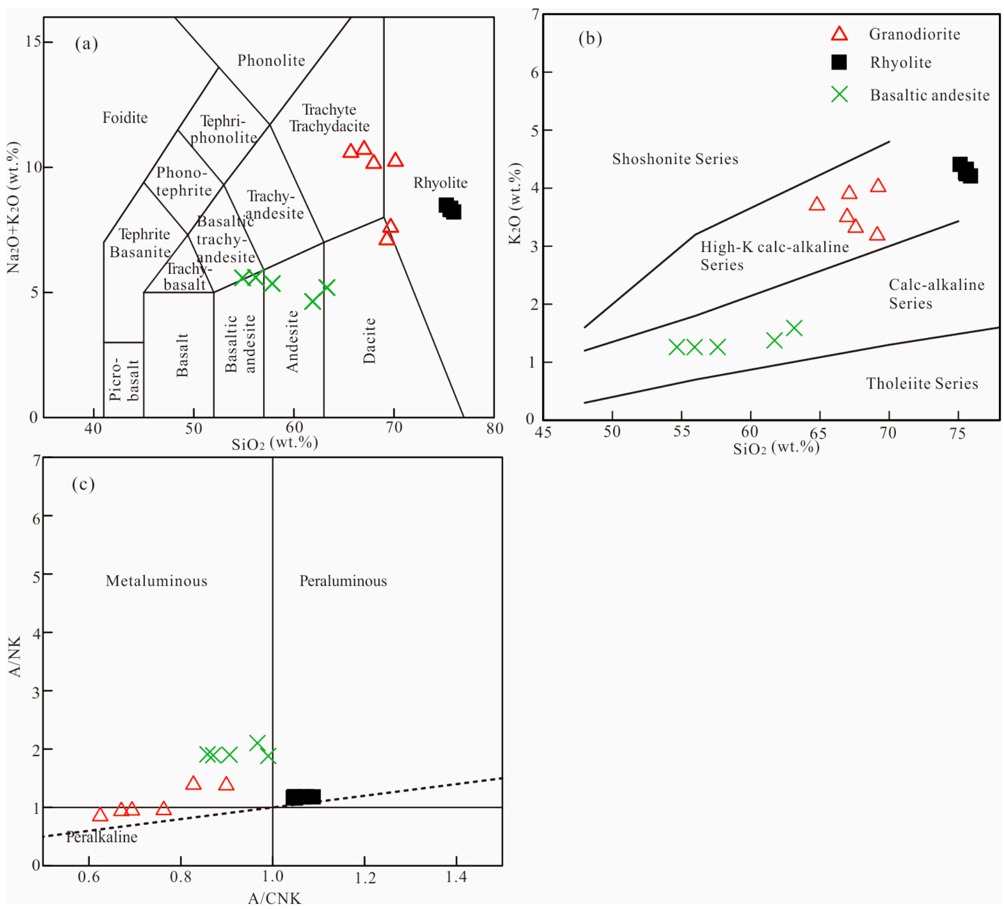

Figure 6. Geochemical classification diagrams for the Zhangfangshan granodiorites and Baishantang bimodal volcanic rocks. (**a**) TAS diagram [57], (**b**) K_2O versus SiO_2 diagram [58], (**c**) A/NK versus A/CNK diagram [59].

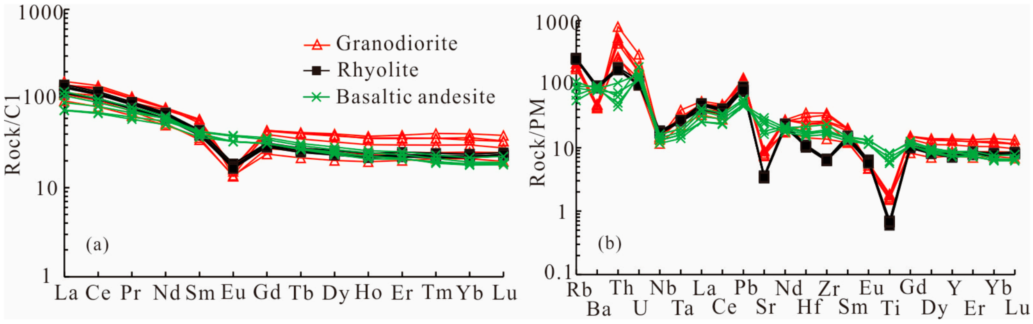

Figure 7. Chondrite (C1)-normalized REE patterns (**a**) and Primitive Mantle (PM)-normalized multi-element diagrams (**b**) for the Zhangfangshan granodiorites and Baishantang bimodal volcanic rocks. C1 and PM values are from Sun and McDonough [60].

5.2.2. Baishantang Bimodal Volcanic Rocks

Baishantang rhyolites have high SiO_2 (75.12~75.87 wt.%), Na_2O (4.00~4.07 wt.%), K_2O (4.21~4.41 wt.%) and $Na_2O + K_2O$ (8.21~8.48 wt.%) contents; moderate Al_2O_3 (13.14~13.53 wt.%) contents; and low ${}^{T}Fe_2O_3$ (1.41~1.74 wt.%), MgO (0.26~0.37 wt.%) and TiO_2 (0.13~0.14 wt.%) contents; their $Mg^{\#}$ values are 23.72~33.58. In the TAS diagram (Figure 6a), all samples are plotted in the rhyolite field in the TAS diagram (Figure 6a) and belong to the high-K calc-alkaline series in the K_2O-SiO_2 diagram (Figure 6b). The A/CNK ratios of all rhyolites are 1.04~1.09 and plotted in the peraluminous (Figure 6c). Rhyolite samples display LREE-enriched REE patterns ($(La/Yb)_N$ = 5.18~6.28, LREEs/HREEs = 5.71~6.55) and have obvious negative Eu anomalies (δEu = 0.48~0.52) (Figure 7a). They are enriched in Rb, Th and Pb; depleted in HREEs and Ba, Nb, Ta, Ti and Sr; and weakly depleted in Zr and Hf (Figure 7b).

Baishantang basaltic andesites have moderate SiO_2 (54.66~63.14 wt.%) contents; high Al_2O_3 (14.36~16.13 wt.%), MgO (3.47~4.26 wt.%), Na_2O (3.25~4.32 wt.%), ${}^{T}Fe_2O_3$ (7.97~10.71 wt.%) and TiO_2 (1.28~1.87 wt.%) contents; and low P_2O_5 (0.40~0.55 wt.%) and K_2O (1.26~1.59 wt.%) contents. The $Mg^{\#}$ values are 44.08~46.30, and the $Na_2O + K_2O$ values are 4.63~5.58 wt.%. The samples belong to calc-alkaline series (Figure 6b). Basaltic andesite samples display LREE-enriched REE patterns ($(La/Yb)_N$ = 3.85~6.49, LREEs/HREEs = 4.09~6.06) and have no obvious negative Eu anomalies (δEu = 0.92~0.99) (Figure 7a). They are enriched in Rb, Ba, Th, U and Pb; weakly enriched in Zr and Hf; and depleted in Nb, Ta and Ti (Figure 7b).

5.3. Whole-Rock Nd-Hf Isotope of the Baishantang Bimodal Volcanic Rocks

Whole-rock Nd-Hf isotopic compositions of Baishantang rocks are plotted in Figure 8. The initial Nd and Hf isotope ratios were calculated using the zircon U-Pb ages (272 Ma). The ${}^{176}Hf/{}^{177}Hf$ ratios of 0.282674~0.282682 and ${}^{143}Nd/{}^{144}Nd$ ratios of 0.512252~0.512264 were measured for three rhyolite samples, which correspond to initial ${}^{176}Hf/{}^{177}Hf$ ratios of 0.282542~0.282549 and initial ${}^{143}Nd/{}^{144}Nd$ ratios of 0.512023~0.512041. They had negative $\varepsilon_{Hf}(t)$ (−2.2~−1.9) and $\varepsilon_{Nd}(t)$ (−5.2~−4.8) values, with two-stage Hf and Nd model ages (T_{DM2}) between 1427~1411 Ma and 1460~1433 Ma, respectively. The ${}^{176}Hf/{}^{177}Hf$ ratios of 0.282721~0.282831 and ${}^{143}Nd/{}^{144}Nd$ ratios of 0.512381~0.512522 were measured for three basaltic andesite samples, which correspond to initial ${}^{176}Hf/{}^{177}Hf$ ratios of 0.282655~0.282760 and initial ${}^{143}Nd/{}^{144}Nd$ ratios of 0.512146~0.512205. Basalitic andesites have a negative $\varepsilon_{Nd}(t)$ (−2.8~−0.4) but positive $\varepsilon_{Hf}(t)$ (1.8~5.5).

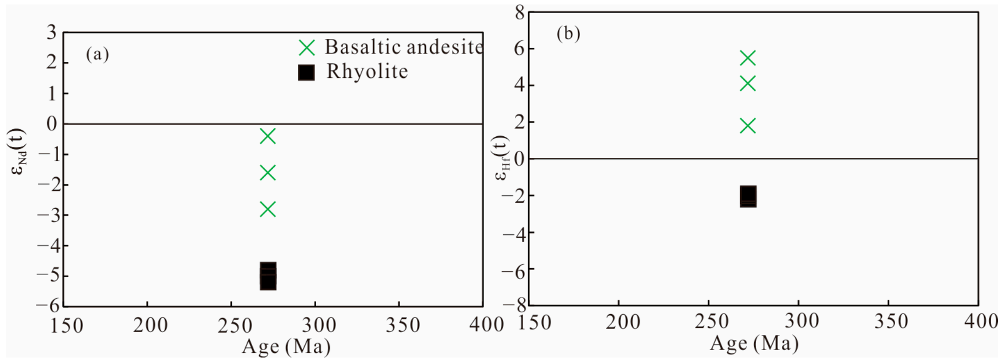

Figure 8. (**a**) $\varepsilon_{Nd}(t)$ values of the Baishantang bimodal volcanic rocks; (**b**) $\varepsilon_{Hf}(t)$ values of the Baishantang bimodal volcanic rocks.

6. Discussion

6.1. Early Permian Magmatism in the SBOB

In this research, we studied granodiorite and obtained new zircon U-Pb ages of 288.7 ± 1.7 Ma. Zircon grains from this pluton are euhedral-subhedral with clear concentric oscillatory patterns, without overgrowth rim and inherited cores (Figure 4a). Meanwhile, these zircons have relatively high Th/U ratios (0.44~0.65), indicative of a magmatic origin. In the field, the Zhangfangshan granodiorite intruded the Zhangfangshan ophiolite (362 Ma) [61], suggesting that the Zhangfangshan granodiorite was formed in the early Permian.

The Baishantang basaltic andesite and rhyolite are spatially associated with each other, and their SiO_2 contents have obvious discontinuity, which clearly suggests that they are likely coeval and, thus, constitute a bimodal volcanic suit. The timing of the Baishantang bimodal volcanic magmatism can be determined by the eruption age of the rhyolite [62]. The basaltic andesite and rhyolite outcrops are in the volcanic section of the Ganquan Formation. The Ganquan Formation is widely distributed in the SBOB and consists of marble and volcanic sections. Through studies, it has been determined that the Ganquan Formation is in contact with the Upper Carboniferous Shibanshan and Lower Permian Shuangbaotang Formations [63]. The fossils in the marble section and the zircon U-Pb isotopic age in the volcanic section indicate that the Ganquan Formation was formed in the late Carboniferous–early Permian while the volcanic section was formed in the early Permian [63]. All the dated zircons in this study exhibit well-developed zoning and have relatively high Th/U ratios (0.46~1.30), indicative of a magmatic origin. Sixteen analyses yielded a concordant age of 272.3 ± 1.6 Ma; this result is consistent with the previous study and is interpreted as the crystallization age of the Baishantang rhyolite. $^{206}Pb/^{207}Pb$ ages of 395 Ma are yield by GQ-LW-3 and GQ-LW-7, clearly older than other ages, and represent the captured zircon ages. Therefore, the Baishantang bimodal volcanic rocks were formed in early Permian.

There are other early Permian magmatisms in the SBOB. Granitic plutons with an age of 290~270 Ma were reported in the Shuwojing, Western Shuwojing, Bandaoshan, Wohushan, Liuyuan and Yinwaxia, including syenogranite, biotite monzogranite, biotite granite, monzogranite and granodiorite [13,27,33,35]. Meanwhile, the ultramafic-mafic rocks and mafic-felsic dykes are also widely distributed in the SBOB, such as Podong, Cihai, Yitiaoshan, Gubaoquan, Yinwaxia and Niujuanzi [26,31,32,34,64–66]. These mafic-felsic rocks, combined with the Zhangfangshan granodiorite and the Baishantang bimodal volcanic rocks studied in this paper, indicate that the early Permian magmatic activities are widespread in the SBOB.

6.2. Petrogensis

6.2.1. The Zhangfangshan Granodiorite

Generally, granites are categorized into I-, S-, A- and M-type granite based on geochemical and mineralogical features [67–69]. Early Permian granodiorites (Ca. 288 Ma) have high K_2O contents (3.20~4.03 wt.%), unlike M-type granites with low K_2O contents (<1 wt.%). Zhangfangshan granodiorites are metaluminous (A/CNK < 1.1), and Al-bearing minerals are lacking (e.g., garnet and andalusite), indicating that Zhangfangshan granodiorites are not S-type granites. Therefore, the Zhangfangshan granodiorites are I- or A-type granites. All granodiorite samples display high K_2O + Na_2O (7.12~10.74 wt.%) and FeO_t contents (2.04~3.47 wt.%), low Rb contents (109.56~134.60 ppm), high 10,000*Ga/Al (2.8~3.3) and Zr + Nb + Ce + Y (368.17~544.83 ppm) values, demonstrating that the Zhangfangshan granodiorites show an affinity to A-type granites [69–74]. In the discrimination diagrams for I-S-A-type granite by Whalen et al. [70] (Figure 9a,b), all samples are plotted in the A-type granite field rather than the I and S-type field. A high calculated zircon saturation temperature is the most typical feature of A-type granite [59,75]. The calculated zircon saturation temperatures of Zhangfangshan granodiorite samples are 895~1004 °C [76], higher than the average temperatures of A- and I-type granites (Figure 9c). In summary, the studied granodiorites can be regarded as A-type granites. Based on different geochemical characteristics, A-type granites can be further divided into A1- and A2-type granites [77]. All samples have high Y/Nb (3.47~5.99), Rb/Nb (10.73~14.51) and Ce/Nb (5.99~8.36) ratios and are plotted within the A2 field in the Nb-Y-Ce diagram (Figure 9d). In conclusion, Zhangfangshan granodiorites are defined as A2-type granites.

Various models have been proposed to illustrate the formation of A-type granites, including the fractionation-crystallization process of mantle-derived alkaline magma [78,79], magma mixing between mafic and felsic magma, and partial melting of the lower continental crust caused by mantle magma underplating [71].

The Zhangfangshan granodiorites have high SiO_2 (64.78~69.21 wt.%) and K_2O (3.20~4.03 wt.%) contents, are enriched in LREEs and have a depletion of HFSEs as well as having negative Sr and Ti anomalies, indicating that the rocks are difficult to be formed by a high differentiation of mantle-derived magma [71]. The Y/Ho ratios (28.40~30.45) of granodiorites are close to those of chondrite (28), and the Zr/Hf ratios (34.7~38.9) of the samples belong to “CHARAC field (Zr/Hf ratios of 26~46)” [71], indicating that the fractional crystallization is limited. Meanwhile, if the felsic rocks were derived from the fractional crystallization of basaltic magma, voluminous mafic rocks should be exposed in the area [80]. However, there are no coeval intermediate-basic rocks exposed in the region. In conclusion, the Zhangfangshan granodiorites were not formed by the fractional crystallization of mantle-derived magmas.

The Ce/Pb (2.56~4.53) and La/Nb (2.60~3.61) values of granodiorites were found to be close to those of the crust (Ce/Pb < 15, La/Nb = 2.2) [81], indicating that the granodiorite had crustal affinity. However, samples also have high MgO contents and $Mg^{\#}$ values (>40, average 46.58), including Na_2O contents greater than or close to those of K_2O. These features are different from those of melts formed by the partial melting of the basaltic lower crust. Meanwhile, the Lu/Yb ratios (0.14~0.15) of these samples are similar to the ratio of the mantle-derived magma (0.15), suggesting a contribution from the mantle. Zhanfangshan granodiorite formation is not solely derived from the partial melting of the lower crust, and the addition of high-Mg mantle-derived mafic magma is required. Due to the strong Quaternary cover, no mafic enclaves have been found in the Zhangfangshan pluton, but we can still find evidence of magma mixing: (a) the obvious zonal structure of plagioclase, the existence of acicular apatite, and the presence of felsic inclusion in plagioclase crystals. These petrological features are special mineral phenomena in rocks formed from magma mixing [82]. (b) Previous studies have suggested that increasing Fe + Mg contents would be expected due to the basification of relatively felsic magma [71]. Zhangfangshan granodiorites display a positive correlation of FeO_t + MgO with TiO_2 (Figure 10a). The samples also have variations in MgO and TFe_2O_3 contents, which favors magma mixing between mantle-derived mafic magma and crust-derived felsic melts [71,83]. (c) The Zhangfangshan granodiorite samples show magma-mixing trends in the 1/V-Rb/V diagram (Figure 10b). Therefore, potential magma mixing may occur in the Zhanfangshan granodiorite formation process.

Granodiorites have the characteristics of depletions of Ba, Eu, Sr, Ti, Nb and Ta and an obvious plagioclase ring structure, which indicate the crystallization differentiation of the granodiorite and fractionation of plagioclase and Ti-bearing phases.

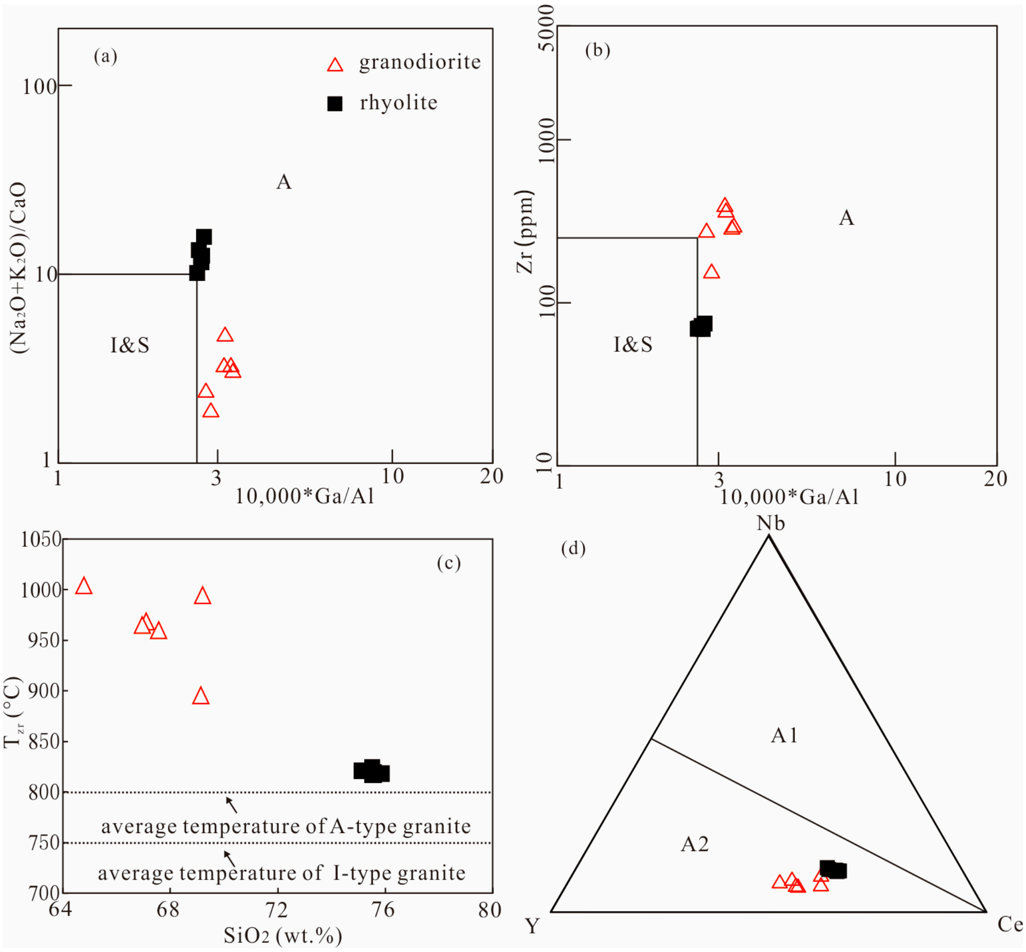

Figure 9. (**a**) ($Na_2O + K_2O$)/CaO and (**b**) Zr vs. 10,000*Ga/Al diagram [79]; (**c**) T_{Zr} (°C) vs. SiO_2 diagram; (**d**) Nb-Y-Ce diagram [77]. I: I-type felsic rock; S: S-type felsic rock; A: A-type felsic rock; A1: A1-type felsic rock; A2: A2-type felsic rock; T_{Zr} (°C): zircon saturation temperature; average temperature of A and I- type granite after [73,84].

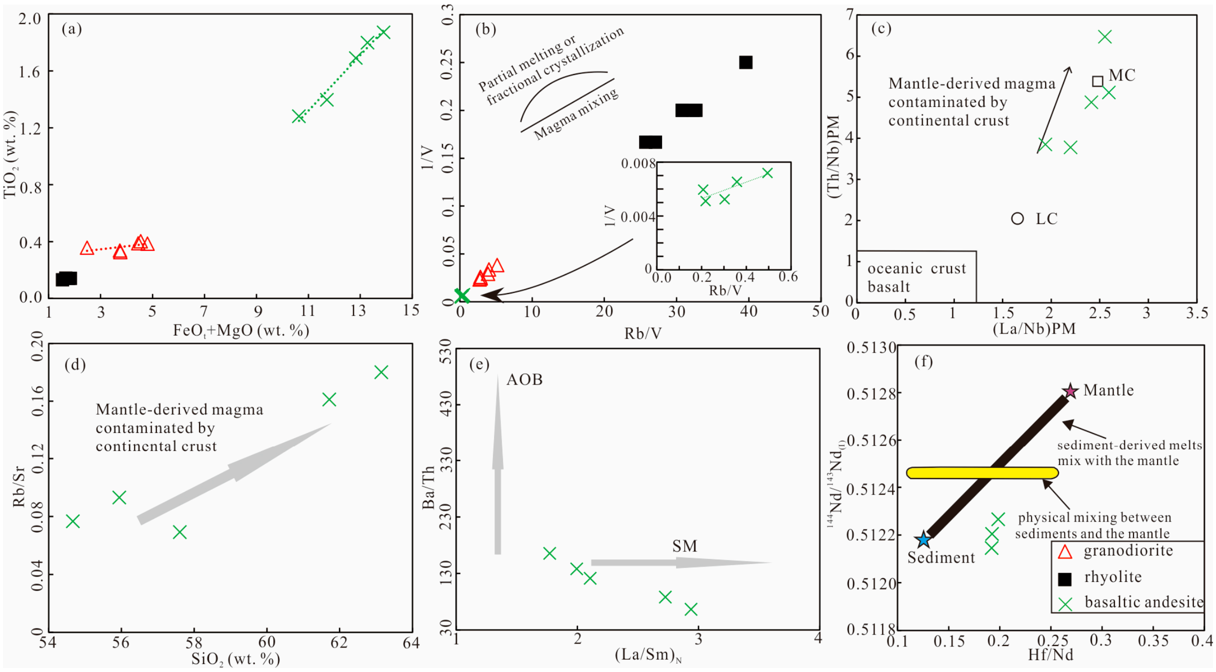

Figure 10. (**a**) TiO_2 vs. FeO_t + MgO diagram [82]; (**b**) 1/V vs. Rb/V diagram [85]; (**c**) $(Th/Nb)_{PM}$ vs. $(La/Nb)_{PM}$ diagram [86]; (**d**) Rb/Sr vs. SiO_2 diagram [87]; (**e**) Ba/Th vs. $(La/Sm)_N$ diagram [88]; (**f**) $^{144}Nd/^{143}Nd(i)$ vs. Hf/Nd diagram [88]. C: crust; M: mantle; Cm: crust-mantle mixed; LC: lower crust; MC: middle crust; AOB: altered oceanic basalt; SM: sediment metasomatism.

6.2.2. The Baishantang Bimodal Volcanic Rocks

The Baishantang rhyolites have the characteristics of being weakly peraluminous (A/CNK are 1.04~1.09) and having no aluminum-rich minerals, indicating that the rhyolites are I- or A-type granites rather than S-type granites. Further, characteristics such as high 10,000*Ga/Al and FeO_t/MgO values (2.60~2.73 and 3.53~5.73); low contents of MgO (0.26~0.37 wt.%) and CaO (0.53~0.82 wt.%); enrichment of Rb, Th and Pb; and depletion of Nb, Ta, Ti, Sr and Ba pertain to an A-type signature. Although the Zr + Nb + Ce + Y values (173.40~356.60 ppm and most of them are less than 350 ppm) are different from values of typical A-type granite (Zr + Nb + Ce + Y > 350 ppm), Baishantang rhyolites also have low Rb contents (154.00~163.50 ppm), high FeO_t contents (1.27~1.57 wt.%) and zircon saturation temperatures (817~824 °C) (Figure 9c), which are different from I-type but similar to A-type felsic rocks. Meanwhile, the almost constant Rb/Sr values of rhyolites (2.13~2.26) show that the Baishantang rhyolites do not belong to highly fractionated felsic rock [89]. In the discrimination diagrams of I-S-A-type granite (Figure 9a,b), all samples are plotted in the A-type field. Therefore, Baishantang rhyolites are A-type felsic rocks. All of these samples have relatively high Y/Nb (2.58~2.69), Ce/Nb (4.87~5.59) and Rb/Nb (11.88~13.69) ratios [71], plotting into the A2 field in the Nb-Y-Ce diagram (Figure 9d). In conclusion, the Baishantang rhyolites are defined as A2-type felsic rocks.

As A2-type felsic rocks, the Baishantang rhyolites have high SiO_2 and K_2O contents, have low MgO contents and $Mg^{\#}$ values, are enriched in LREEs, and are depleted in HFSEs, Sr and P. These characteristics indicate that rhyolites are difficult to form through the high differentiation of mantle-derived magma. The Y/Ho ratios (25.51~26.69) of the samples are close to those of chondrite, indicating that their fractional crystallization is limited [71]. Meanwhile, the exposed area of the rhyolite is much larger than that of the basaltic andesite. Therefore, the Baishantang rhyolite is probably derived from the partial melting of crustal or magma mixing rather than the crystallization differentiation of mantle-derived magma. A-type felsic rocks formed through magma mixing between crust- and mantle-derived magma generally exhibit a wide range of geochemical and isotopic compositions [83]. However, the samples have stable and high SiO_2 contents and low MgO contents and $Mg^{\#}$ values; the Cr (1.00~8.00 ppm) and Ni (1.20~4.40 ppm) contents are also obviously lower than those of mantle-derived magma (Cr = 300~500 ppm, Ni = 300~400 ppm) [60]. These features illustrate that the Baishantang rhyolite could not be formed through magma mixing. Although the samples show a positive correlation in the 1/V-Rb/V diagram (Figure 10b), the rhyolites have homogeneous and negative ε_{Nd}(t) and ε_{Hf}(t) values (Figure 8), and no special mineral phenomenon can be observed in the photomicrographs, implying that magma mixing is not the genesis of the rhyolites. The Ce/Pb (4.01~4.99), Lu/Yb (0.15~0.16), Nd/Th (1.94~2.14) and Nb/U (5.46~6.30) ratios of Baishantang rhyolites are different from those of mantle-derived magma but close to the average ratios of the crust (Ce/Pb < 15, 0.16 < Lu/Yb < 0.18, Nd/Th = 3, Nb/U = 9.7) [60,81], indicating that the rhyolite has crustal affinity. The Baishantang rhyolites have negative ε_{Nd}(t) and ε_{Hf}(t) values, and the two-stage model ages (T_{DM2}) of Nd and Hf are 1460~1433 Ma and 1411~1427 Ma, which are larger than the crystallization age of rhyolites. Studies have shown that if the ε_{Nd}(t) (ε_{Hf}(t)) of intermediate-felsic rocks is negative, and the two-stage model age is much larger than its crystallization age, then the rocks originated from the partial melting of ancient crust, and the zircon age represents the reconstruction time of the crust [90–92]. There are Mesoproterozoic crustal materials in the SBOB, such as the Jiujing biotite plagioclase gneiss (1408 $\pm$ 4 Ma) [18] and the Gubaoquan paragneiss (detrital zircon age ~1.4 Ga) [93]. The two-stage model ages of the rhyolites are consistent with the previous results, suggesting that the Baishantang rhyolite is related to the partial melting of ancient continental crust [94]. The rhyolite samples show depletions in Eu, Ba, Nb, Ta, Sr and Ti, which could be due to the fractionation of plagioclase and Ti-bearing phases [26].

The Baishantang basaltic andesite has high contents of MgO, Al_2O_3, Na_2O, ${}^{T}Fe_2O_3$ and TiO_2, has low contents of P_2O_5 and K_2O, and belongs to the calc-alkaline series (Figure 6b). These high $Mg^{\#}$ values (44.08~46.30) are in contrast to the magma produced through partial melting of the basic lower crust (in which the $Mg^{\#}$ value is lower than 45). The Lu/Yb ratios (0.15) are similar to the mantle value (Lu/Yb = 0.15) [60], indicating the mantle's origin. However, these rocks display low Ce/Pb ratios (4.51~8.75) and Nd/Th ratios (3.33~6.95), which are close to the values of the continental crust (Ce/Pb < 15, Nd/Th $\approx$ 3) [95], and they are depleted in HFSEs (Nb, Ta, Ti) while being enriched in LILEs (Rb, Ba, Th, U and Pb), implying the influence of crustal material on magma. The Nb/Ta and high $(Th/Nb)_{PM}$ ratios are considered to be important parameters for crustal contamination [96,97]. The $(Th/Nb)_{PM}$ values of these samples are 3.78~6.47, larger than 1 [98], and the Nb/Ta values (14.15~14.56) for basaltic andesites are between those of the mantle (17.5 $\pm$ 2.5) and the crust (11.4) [60,92]. Meanwhile, all basaltic andesites have extremely heterogeneous isotopic signatures (Figure 8) and are plotted along the mantle-derived magma contaminated by the continental crust trend as shown in the $(La/Nb)_{PM}$–$(Th/Nb)_{PM}$ and Rb/Sr-SiO_2 diagrams (Figure 10c,d). All these features indicate that the magmas were modified by crustal materials during magma emplacement. Baishantang basaltic andesites have negative ε_{Nd}(t) but positive ε_{Hf}(t) values, which seems to indicate an opposite mantle source region (enriched mantle for ε_{Nd}(t) but depleted mantle for εHf(t)). According to the formula for the crust Nd-Hf isotope (ε_{Hf}(t) = 1.34 $\times$ ε_{Nd}(t) + 2.82) [98], the actual ε_{Hf}(t) values are obviously larger than the values coupled with the whole rock ($-$0.93~2.28), and Nd-Hf isotopes are decoupled. Several mechanisms that can lead to Nd-Hf isotopic decoupling: (1) deeply subducted oceanic basalt [99]; (2) the lower crust that has undergone an ancient anataxis with residual phases of garnet and zircon may be an optional reservoir [88,100,101]; (3) mixing of components with different geochemical features [88,102–104]. The magmatic rock formed by the melting of basaltic crust has lower $Mg^{\#}$ ($Mg^{\#}$ < 45) values [105] and obvious differentiation between MREE and HREE during anatexis [102]. The features of Baishantang basaltic andesites, such as high $Mg^{\#}$ values and weak differentiation between MREEs and HREEs ($(Dy/Yb)_N$ = 1.28~1.40), contradict the idea that decoupling was caused by deeply subducted ocean basalt or the lower crust undergoing an ancient anatexis event.

Nd-Hf isotopic decoupling may result from the mixing of components with different geochemical features. As discussed above, the crustal material played an important role in the basaltic andesite formation (Figure 10c,d). Basaltic andesites have high $(La/Sm)_N$ ratios and low Ba/Th values (Figure 10e), which are thought to reflect sediment involvement. The influence of sediments on magma can be classified as sediment-derived melt mixing and physical mixing. The $(^{143}Nd/^{144}Nd)$–(Hf/Nd) diagram (Figure 10f) can distinguish between these two models [106]. All samples are distributed along an oblique line rather than a horizontal line (Figure 10f), indicating that sediment-derived melt mixing, rather than physical mixing between sediments, and mantle-derived magma play an important role in basaltic andesites formation. The partial melting of the mantle mixed with sediment-derived melts or bulk subducted sediments could generate magmas with Nd-Hf isotopic decoupling [88]. Therefore, the Nd-Hf isotopic decoupling of basaltic andesite is a result of the mixing of sediment-derived melts and mantle magma.

The Dy/Yb values of basaltic andesites are 1.92~2.09. These values are between the spinel lherzolite mantle melts (<1.5) and garnet lherzolite mantle melts (>2.5), indicating that the magma comes from the partial melting of the two [107]. The transformation depth of the spinel and garnet is 70~80 km [108], and it is speculated that the formation depth of basaltic andesite magma is about 70~80 km.

6.3. Tectonic Implications

The late Paleozoic tectonic setting of the SBOB and the closure time of the PAO are the focus of this research. Paleozoic magmatic rocks are widely distributed in the SBOB, which record the subduction, closure and post-collision evolution history of the PAO. The Xiaoquandong 395 Ma A-type granite and Hongliuhe 404 Ma A-type granite intruded into the Hongliuhe ophiolite in the SH unit, indicating that the HNY ocean closed before the early Devonian [44,109,110]. Magmatism in the SH and Shibanshan units after early Devonian indicate the evolution process of the back-arc basin represented by the HZ ophiolitic belt [44]. Late Devonian–early Carboniferous arc magmatism occurred in the Tanshanzidong, Huaniushan and Shuangfengshan in the SH unit [44], but it did not occur in the Shibanshan unit, indicating the northward subduction of the HZ ocean during this time [94].

Late Carboniferous to early Permian magmatic rocks are widely distributed in the Shibanshan and SH units, constituting the main magmatic events during the late Paleozoic. Qiaowan 304 Ma granite [27], Liuyuan and Shuwojing 285~275 Ma granite [12,13] and Yinwaxia 273 Ma rhyolite [111], and other acidic rocks, are the main types of late Carboniferous–early Permian magmatic rocks in the SBOB. These rocks have the geochemical characteristics of calc-alkaline to high K calc-alkaline and belong to highly differentiated I- or A-type felsic rocks. Except for these felsic rocks, the Podong, Cihai and Niujuanzi 282~280 Ma tholeiite-Calc-alkaline series diabase and other mafic rocks are also widely distributed in the SBOB [64–66]. These felsic and mafic rocks were formed in the extensional tectonic setting [12,13,64–66,111]. The A1-type felsic rocks were formed in the non-orogenic but the A2-type in syn-collision or post-collision tectonic environments [77]. The Zhangfangshan granodiorite and Baishantang rhyolite are A2-type felsic rocks, and all samples are plotted in the POG field in the Nb-Y and Ta-Yb diagrams (Figure 11a,b), suggesting the post-collision tectonic setting. Baishantang basaltic andesites have high Zr (180~258 ppm) concentrations and Zr/Y (5.37~6.53) ratios, similar to basalts formed in the within-plate extensional setting (Zr > 70 ppm and Zr/Y > 3) [112]. All basaltic andesite samples are plotted in the WPB field in the Zr/Y-Zr and Ti-Zr diagrams (Figure 11c,d), suggesting a within-plate extensional environment. The formation age and tectonic setting of the granodiorites and the bimodal volcanic rocks in this study are similar to late Carboniferous–early Permian magmatic rocks, showing that the late Carboniferous–early Permian magmatism in the SBOB were formed in the same tectonic environment. Meanwhile, intermediate-basic dikes in 282~280 Ma are widely distributed in the SBOB, indicating an extensional tectonic background caused by lithospheric delamination [25,26]. Based on the regional stratigraphic, the late Carboniferous to early middle Permian in the SBOB is a continuous transgressive sedimentary sequence, and there is no unconformity interface reflecting the continental crust of the SBOB, which was further stretched on the basis of a post-collisional extension in the late Carboniferous [63,113–115]. Therefore, combined with magmatism and stratigraphic characteristics in the SBOB, the HZ ocean has been closed, and the SBOB was in a post-collisional extensional setting during early Permian (Figure 12).

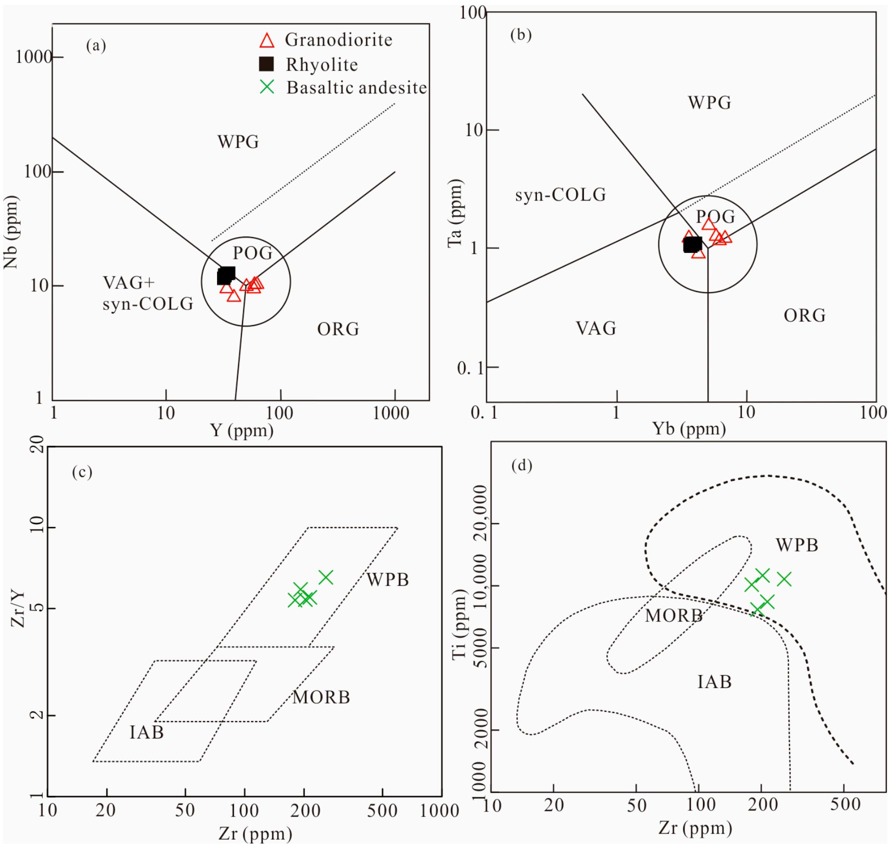

Figure 11. Tectonic setting discrimination diagrams for the Zhangfangshan granodiorite and the Baishantang bimodal volcanic rocks: (**a**) Nb vs. Y diagram [116]; (**b**) Ta vs. Yb diagram [116]; (**c**) Zr/Y vs. Zr diagram [117]; (**d**) Ti vs. Zr diagram [117]. MORB: mid-ocean ridge basalt; IAB: island-arc basalt; WPB: within-plate basalt; VAG: volcanic arc granite; POG: post-orogenic granite; ORG: ocean ridge granite; WPG: within-plate granite; syn-COLG: syn-collisional granite.

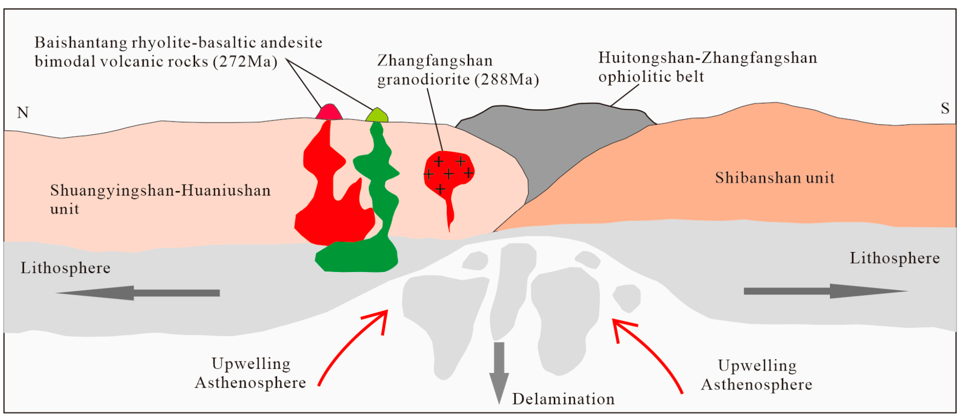

Figure 12. Schematic illustration of the proposed genetic model for the early Permian in the Southern Beishan Orogenic Belt.

7. Conclusions

A petrographic, geochronological, whole-rock major-oxides, trace-element and Nd-Hf isotopic study of the Zhangfangshan granodiorite and the Baishantang bimodal volcanic rocks in the SBOB led to the following conclusions.

1. The Zhangfangshan granodiorites have $^{206}Pb/^{238}U$ ages of 288.7 ± 1.7 Ma, and the Baishantang rhyolites have $^{206}Pb/^{238}U$ ages of 272.3 ± 1.6 Ma.
2. The Zhangfangshan granodiorite belong to the A2-type granite and are generated from magma mixing between mafic and felsic magmas.
3. The Baishantang rhyolites belong to the A2-type granite and are generated from the partial melting of crust. The Baishantang basaltic andesites belong to the calc-alkaline series, which originated from the partial melting of the mantle and mixing via sediment-derived melts.
4. The Zhangfangshan granodiorites and the Baishantang bimodal volcanic rocks were formed in the post-collision extensional setting. The SBOB was in the post-collision period, and the HZ ocean was closed before the early Permian.

Supplementary Materials: The following supporting information can be downloaded at: https://www.mdpi.com/article/10.3390/min13121468/s1, Table S1: Results of U-Pb dating using zircons from the Zhangfangshan granodiorites and the Baishantang bimodal volcanic rocks; Table S2: Whole-rock major (wt.%) and trace-element (ppm) analyses of the Zhangfangshan granodiorites and the Baishantang bimodal volcanic rocks; Table S3: Whole-rock Nd-Hf isotopic data of the Baishantang bimodal volcanic rocks.

Author Contributions: Methodology, L.W., X.Z., E.W. and J.Z.; Investigation, L.W., E.W., W.C., G.S., F.Z. and H.W.; Resources, L.W.; Data curation, L.W., E.W., W.C., G.S., F.Z. and H.W.; Writing—original draft, L.W.; Writing—review and editing, X.Z., J.Z. and J.W.; Project administration, J.W.; Funding acquisition, X.Z. and J.W. All authors have read and agreed to the published version of the manuscript.

Funding: This research was supported by the China Atomic Energy Authority (CAEA) through the Geological Disposal Program and the National Second Expedition to the Tibetan Plateau (2019QZKK0901).

Data Availability Statement: The original contributions presented in the study are included in the article/Supplementary Material.

Acknowledgments: We would like to thank Conghui Xiong and Xiaoli Yan for their valuable help with the analysis, Honggang Zhao for his help on the field. We sincerely thank the editors and all reviewers for their valuable feedback that we have used to improve the quality of our manuscript.

Conflicts of Interest: The authors declare no conflict of interest.

References

1. Briggs, S.M.; Yin, A.; Manning, C.E.; Chen, Z.L.; Wang, X.F.; Grove, M. Late Paleozoic tectonic history of the Ertix Fault in the Chinese Altai and its implications for the development of the Central Asian Orogenic System. *Geol. Soc. Am. Bull.* **2007**, *119*, 944–960. [CrossRef]
2. Briggs, S.M.; Yin, A.; Manning, C.E.; Chen, Z.L.; Wang, X.F. Tectonic development of the southern Chinese Altai Range as determined by structural geology, thermobarometry, 40Ar/39Ar thermochronology, and Th/Pb ion microprobe monazite geochronology. *Geol. Soc. Am. Bull.* **2009**, *121*, 1381–1393. [CrossRef]
3. Şengör, A.M.C.; Natal'in, B.A.; Burtman, V.S. Evolution of the Altaid tectonic collage and Palaeozoic crustal growth in Eurasia. *Nature* **1993**, *364*, 299–307. [CrossRef]
4. Jahn, B.M.; Wu, F.Y.; Chen, B. Granitoids of the Central Asian Orogenic Belt and continental growth in the Phanerozoic. *Geol. Soc. Am. Spec. Pap.* **2000**, *350*, 181–193.
5. Windley, B.F.; Alexeiev, D.; Xiao, W.; Kroner, A.; Badarch, G. Tectonic models for accretion of the Central Asian Orogenic Belt. *J. Geol. Soc. Lond.* **2007**, *164*, 31–47. [CrossRef]
6. Xiao, W.J.; Pirajno, F.; Seltmann, R. Geodynamicsand metallogeny of the Altaid orogen. *J. Asian Earth Sci.* **2008**, *32*, 77–81. [CrossRef]
7. Khain, E.V.; Bibikova, E.V.; Kröner, A.; Zhuravlev, D.Z.; Sklyarov, E.V.; Fedotova, A.A.; Kravchenko-Berezhnoy, I.R. The most ancient ophiolite of the Central Asian fold belt: U-Pb and Pb-Pb zircon ages for the Dunzhugur Complex, Eastern Sayan, Siberia, and geodynamic implications. *Earth Planet. Sci. Lett.* **2002**, *199*, 311–325. [CrossRef]

8. Chen, X.H.; Dong, S.W.; Shi, W.; Ding, W.C.; Zhang, Y.P.; Li, B.; Shao, Z.G.; Wang, Y. Construction of the continental Asia in Phanerozoic: A review. *Acta Geol. Sin.* **2022**, *96*, 26–51. (In Chinese with English abstract) [CrossRef]
9. Xiao, W.J.; Song, D.F.; Windley, B.F.; Li, J.L.; Han, C.M.; Wan, B.; Zhang, J.E.; Ao, S.J.; Zhang, Z.Y. Accretionary processes and metallogenies of the Central Asian Orogenic Belt. Advances and perspectives. Science China. *Earth Sci.* **2020**, *63*, 329–361. [CrossRef]
10. Huang, H.; Wang, T.; Tong, Y.; Qin, Q.; Ma, X.X.; Yin, J.Y. Rejuvenation of ancient micro-continents during accretionary orogenesis: Insights from the Yili Block and adjacent regions of the SW Central Asian Orogenic Belt. *Earth-Sci. Rev.* **2020**, *208*, 103255. [CrossRef]
11. Şengör, A.M.C.; Natal'in, B.A.; Sunal, G.; Van der Voo, R. The tectonics of the Altaids: Crustal growth during the construction of the continental lithosphere of central asia between ∼750 and ∼130 Ma ago. *Annu. Rev. Earth Planet. Sci.* **2018**, *46*, 439–494. [CrossRef]
12. Li, S.; Wilde, S.A.; Wang, T. Early Permian post-collisional high-K granitoids from Liuyuan area in southern Beishan orogen, NW China: Petrogenesis and tectonic implications. *Lithos* **2013**, *179*, 99–119. [CrossRef]
13. Zhang, W.; Pease, V.; Meng, Q.P.; Zheng, R.G.; Thomsen, T.B.; Wohlgemuth-Ueberwasser, C.; Wu, T.R. Timing, petrogenesis, and setting of granites from the southern Beishan late Palaeozoic granitic belt, Northwest China and implications for their tectonic evolution. *Int. Geol. Rev.* **2015**, *57*, 1975–1991. [CrossRef]
14. Zheng, R.G.; Li, J.Y.; Zhang, J.; Xiao, W.J. A prolonged subduction-accretion in the southern Central Asian Orogenic Belt: Insights from anatomy and tectonic affinity for the Beishan complex. *Gondwana Res.* **2021**, *95*, 88–112. [CrossRef]
15. Xiao, W.J.; Mao, Q.G.; Windley, B.F.; Han, C.M.; Qu, J.F.; Zhang, J.E.; Ao, S.J.; Guo, Q.Q.; Cleven, N.R.; Lin, S.F.; et al. Paleozoic multiple accretionary and collisional processes of the Beishan orogenic collage. *Am. J. Sci.* **2010**, *310*, 1553–1594. [CrossRef]
16. Li, J.; Wu, C.; Chen, X.H.; Zuza, A.V.; Haproff, P.J.; Yin, A.; Shao, Z.G. Tectonic evolution of the Beishan orogen in central Asia: Subduction, accretion, and continent-continent collision during the closure of the Paleo-Asian Ocean. *Geol. Soc. Am. Bull.* **2023**, *135*, 5–6. [CrossRef]
17. Yuan, Y.; Zong, K.Q.; Cawood, P.A.; Cheng, H.; Yu, Y.Y.; Guo, J.L.; Liu, Y.S.; Hu, Z.C.; Zhang, W.; Li, M. Implication of Mesoproterozoic (∼1.4 Ga) magmatism within microcontinents along the southern Central Asian Orogenic Belt. *Precambrian Res.* **2019**, *327*, 314–326. [CrossRef]
18. He, Z.Y.; Sun, L.X.; Mao, L.J.; Zong, K.Q.; Zhang, Z.M. Zircon U-Pb and Hf isotopic study of gneiss and granodiorite from the southern Beishan orogenic collage: Mesoproterozoic magmatism and crustal growth. *Chin. Sci. Bull.* **2015**, *60*, 389–399. (In Chinese with English abstract) [CrossRef]
19. Wang, B.R.; Yang, X.S.; Li, S.C.; Teng, C.; Yang, X.J.; Huang, F.Y.; Zhang, X.F.; Cao, J.; Zhou, Y.; Zhang, H.C.; et al. Geochronology, geochemistry, and tectonic implications of early Neoproterozoic granitic rocks from the eastern Beishan Orogenic Belt, southern Central Asian Orogenic Belt. *Precambrian Res.* **2021**, *352*, 106016. [CrossRef]
20. Soldner, J.; Yuan, C.; Schulmann, K.; Štípská, P.; Jiang, Y.; Zhang, Y.; Wang, X. Grenville an evolution of the Beishan Orogen, NW China: Implications for development of an active Rodinian margin. *Geol. Soc. Am. Bull.* **2020**, *132*, 1657–1680. [CrossRef]
21. Lv, C.L.; Yang, F.Q.; Luo, J.S.; Ma, W.F.; Liu, W.X.; Shi, W.M. Isotopic age of rock mass in Gongpoquan mining area in Beishan of Gansu and its geological significance. *Miner. Resour. Geol.* **2021**, *35*, 83–89. (In Chinese with English abstract)
22. Song, D.F.; Xiao, W.J.; Han, C.M.; Tian, Z.H. Geochronological and geochemical study of gneiss schist complexes and associated granitoids, Beishan Orogen, southern Altaids. *Int. Geol. Rev.* **2013**, *55*, 1705–1727. [CrossRef]
23. Yuan, Y.; Zong, K.Q.; He, Z.Y.; Klemd, R.; Jiang, H.Y.; Zhang, W.; Liu, Y.S.; Hu, Z.C.; Zhang, Z.M. Geochemical evidence for Paleozoic crustal growth and tectonic conversion in the Northern Beishan Orogenic Belt, southern Central Asian Orogenic Belt. *Lithos* **2018**, *302–303*, 189–202. [CrossRef]
24. Zhao, K.Q.; Ma, S.M.; Xi, M.J.; Yang, J.Z.; Cai, Y.W.; Gong, J.J. The LA-ICP-MS Zircon U-Pb ages and geochemical characteristics of Late Paleozoic intermediate-acidic intrusive complexes in Shibanjing area, Beishan Mountains, Inner Mongolia, and their geological significance. *Dizhi Lunping* **2020**, *66*, 69–87. (In Chinese with English abstract)
25. Zheng, R.G.; Li, J.Y.; Zhang, J.; Xiao, W.J.; Wang, Q.J. Permian oceanic slab subduction in the southmost of Central Asian Orogenic Belt: Evidence from adakite and high-Mg diorite in the southern Beishan. *Lithos* **2020**, *358*, 105406. [CrossRef]
26. Zhang, Y.Y.; Yuan, C.; Sun, M.; Long, X.P.; Xia, X.P.; Wang, X.Y.; Huang, Z.Y. Permian doleritic dikes in the Beishan Orogenic Belt, NW China: Asthenosphere–lithosphere interaction in response to slab break-off. *Lithos* **2015**, *233*, 174–192. [CrossRef]
27. Zhang, W.; Wu, T.R.; Zheng, R.G.; Feng, J.C.; Luo, H.L.; He, Y.K.; Xu, C. Post-collisional Southeastern Beishan granites: Geochemistry, geochronology, Sr–Nd–Hf isotopes and their implications for tectonic evolution. *J. Asian Earth Sci.* **2012**, *58*, 51–63. [CrossRef]
28. Su, B.X.; Qin, K.Z.; Patrick, A.S.; Liu, P.P.; Tang, D.M.; Malaviarachchi, S.P.K.; Xiao, Q.H.; Sun, H.; Dai, Y.C.; Hu, Y. Geochemistry and geochronology of acidic rocks in the Beishan region, NW China: Petrogenesis and tectonic implications. *J. Asian Earth Sci.* **2011**, *41*, 31–43. [CrossRef]
29. Chen, S.; Guo, Z.J.; Qi, J.F.; Zhang, Y.Y.; Georgia, P.; David, J.W.P. Early Permian volcano-sedimentary successions, Beishan, NW China: Pepe rites demonstrate an evolving rift basin. *J. Volcanol. Geotherm. Res.* **2016**, *309*, 31–44. [CrossRef]
30. Zuo, G.C.; Zhang, S.L.; He, G.Q.; Zhang, Y. Plate tectonic characteristics during the early Paleozoic in Beishan near the Sino-Mongolian border region, China. *Tectonophysics* **1991**, *188*, 385–392. [CrossRef]

31. Xiao, W.J.; Windley, B.F.; Allen, M.B.; Han, C.M. Paleozoic multiple accretionary and collisional tectonics of the Chinese Tianshan orogenic collage. *Gondwana Res.* **2013**, *23*, 1316–1341. [CrossRef]
32. Wang, Y.H.; Zhang, F.F.; Li, B.C.; Xue, C.J.; Liu, J.J.; Zhao, Y.; Zhang, W. Geology and genesis of the Cihai mafic intrusions in Beishan Terrane, Xinjiang, Northwest China: Implication for iron mineralization and tectonic setting. *Ore Geol. Rev.* **2020**, *121*, 103573. [CrossRef]
33. Yu, S.; Zhao, B.B.; Jia, X.; Zhai, X.W.; Ren, J.D. Geochemistry, Geochronology Characteristics and Tectonic Significance of Yitiaoshan Diorite in the Southern Margin of Beishan Orogenic Belt. *Northwest. Geol.* **2022**, *55*, 267–279. (In Chinese with English abstract)
34. Luo, X.Q. Geochemistry and Geochronology of Wohushan Early Permian Syenogranite in the Southern Belt of the Beishan mountains. *Gansu Geol.* **2022**, *31*, 7–16, (In Chinese with English abstract).
35. Guo, X.G.; Chen, S.Y.; Gou, R.; Liu, X.; Wang, Q.; Pu, Q.L. Geochemistry, Chronology and Genesis of Marine Basalts in HouhongquanArea, Beishan, Gansu and Inner Mongolia. *Earth Sci.* **2021**, *46*, 3945–3964. (In Chinese with English abstract)
36. Zhang, W.; Feng, J.C.; Zheng, R.G.; Wu, T.R.; Luo, H.L.; He, Y.K.; Jing, X. LA-ICP MS zircon U–Pb ages of the granites from the south of Yin'aoxia and their tectonic significances. *Acta Petrol. Sin.* **2011**, *27*, 1649–16661. (In Chinese with English abstract)
37. Wang, J.T.; Dong, Y.P.; Zeng, Z.C.; Yang, Z.; Sun, S.S.; Zhang, F.F.; Zhou, B.; Sun, J.P. Geochronology, geochemistry and geological significance of the Huangcaotan pluton in the southern Beishan Orogenic Belt. *Geoscience* **2016**, *30*, 937–949. (In Chinese with English abstract)
38. Ao, S.J.; Xiao, W.J.; Han, C.M.; Li, X.H.; Qu, J.F.; Zhang, J.E.; Guo, Q.Q.; Tian, Z.H. Cambrian to early Silurian ophiolite and accretionary processes in the Beishan collage, NW China: Implications for the architecture of the Southern Altaids. *Geol. Mag.* **2012**, *149*, 606–625. [CrossRef]
39. Tian, Z.; Xiao, W.; Windley, B.F.; Lin, L.N.; Han, C.; Zhang, J.E.; Wan, B.; Ao, S.; Song, D.; Feng, J. Structure, age, and tectonic development of the Huoshishan-Niujuanzi ophiolitic mélange, Beishan, southernmost Altaids. *Gondwana Res.* **2014**, *25*, 820–841. [CrossRef]
40. Su, B.X.; Qin, K.Z.; Santosh, M.; Sun, H.; Tang, D. The Early Permian mafic-ultramafic complexes in the Beishan Terrane, NW China: Alaskan-type intrusives or rift cumulates? *J. Asian Earth Sci.* **2013**, *66*, 175–187. [CrossRef]
41. Hou, Q.Y.; Wang, Z.; Liu, J.B.; Wang, J.; Li, D.P. Geochemistry Characteristics and SHRIMP Dating of Yueyashan Ophiolite in Beishan Orogen. *Geoscience* **2012**, *26*, 1008–1018. (In Chinese with English abstract)
42. Zuo, G.C.; Zhang, S.L.; He, G.Q.; Zhang, Y. Early Paleozoic Plate Tectonics in Beishan Area. *Sci. Geol. Sin.* **1990**, *25*, 305–314+411. (In Chinese with English abstract)
43. Niu, Y.Z.; Shi, G.R.; Wang, J.Q.; Liu, C.Y.; Zhou, J.L.; Lu, J.C.; Song, B.; Xu, W. The closing of the southern branch of the Paleo-Asian Ocean: Constraints from sedimentary records in the southern Beishan Region of the Central Asian Orogenic Belt, NW China. *Mar. Pet. Geol.* **2021**, *124*, 104791. [CrossRef]
44. Wang, H.T. Tectono-Magmatism and Its Geological Significance in the Beishan Area of the Southern Part of the Central Asian Orogenic Belt. Ph.D. Thesis, Lanzhou University, Lanzhou, China, 2019. (In Chinese with English abstract)
45. BGGP. *Hongliudaquan Regional Geological Survey Report (1:200,000)*; Gansu Bureau of Geology: Gansu, China, 1971. (In Chinese with English abstract)
46. BGGP. *Shibanquan Regional Geological Survey Report (1:50,000)*; Gansu Bureau of Geology: Gansu, China, 2013. (In Chinese with English abstract)
47. Song, B.; Zhang, Y.H.; Wan, Y.S.; Jian, P. Mount Making and Procedure of the SHRIMP Dating. *Geol. Rev.* **2002**, *48*, 26–30. (In Chinese with English abstract)
48. Wiedenbeck, M.; Hanchar, J.M.; Peck, W.H.; Sylvester, P.; Vley, J.; Whitehouse, M.; Kronz, A.; Morishita, Y.; Nasdala, L.; Fiebig, J.; et al. Further characterisation of the 91500 zircon crystal. *Geostand. Geoanal. Res.* **2004**, *28*, 9–39. [CrossRef]
49. Pearce, N.J.G.; Perkins, W.T.; Westgate, J.A.; Gorton, M.P.; Chenery, S.P. A Compilation of New and Published Major and Trace Element Data for NIST SRM 610 and NIST SRM 612 Glass Reference Materials. *Geostand. Newsl.* **1997**, *21*, 115–144. [CrossRef]
50. Jackson, S.E.; Pearson, N.J.; Griffin, W.L.; Belousova, E.A. The application of laser ablation-inductively coupled plasma-mass spectrometry to in situ U–Pb zircon geochronology. *Chem. Geol.* **2004**, *211*, 47–69. [CrossRef]
51. Vermeesch, P. IsoplotR: A free and open toolbox for geochronology. *Geosci. Front.* **2018**, *9*, 1479–1493. [CrossRef]
52. Yuan, H.L.; Gao, S.; Liu, X.M.; Li, H.M.; Gunther, D.; Wu, F.Y. Accurate U–Pb age and trace element determinations of zircon by laser ablation-inductively coupled plasma-mass spectrometry. *Geostand. Geoanal. Res.* **2004**, *28*, 353–370. [CrossRef]
53. Li, X.H.; Liu, Y.; Tu, X.L.; Hu, G.Q.; Zeng, W. Precise determination of chemical compositions in silicate rocks using ICP-AES and ICP-MS: A comparative study of sample digestion techniques of alkali fusion and acid dissolution. *Geochimica* **2002**, *31*, 289–294.
54. Gao, J.J.; Liu, J.H.; Li, X.G.; Yan, Q.S.; Wang, X.J.; Wang, H.M. The determination of 52 elements in marine geological samples by an inductively coupled plasma optical emission spectrometry and an inductively coupled plasma mass spectrometry with a high-pressure closed digestion method. *Acta Oceanol. Sin.* **2017**, *36*, 113–121. [CrossRef]
55. Bao, Z.; Zong, C.; Fang, L.; Yuan, H.; Chen, K.; Dai, M. Determination of Hf-Sr-Nd isotopic ratios by MC-ICP-MS using rapid acid digestion after flux-free fusion in geological materials. *Acta Geochim.* **2018**, *37*, 244–256. [CrossRef]
56. Wu, Y.B.; Zheng, Y.F. Genetic mineralogy of zircon and its constraints on U-Pb dating interpretation. *Chin. Sci. Bull.* **2004**, *49*, 1589–1604, (In Chinese with English abstract). [CrossRef]

57. Winchester, J.A.; Floyd, P.A. Geochemical discrimination of different magma series and their differentiation products using immobile elements. *Chem. Geol.* **1977**, *20*, 325–343. [CrossRef]
58. Rickwood, P.C. Boundary lines within petrologic diagrams which use oxides of major and minor elements. *Lithos* **1989**, *22*, 247–263. [CrossRef]
59. Maniar, P.D.; Piccoli, P.M. Tectonic discrimination of granitoids. *Geol. Soc. Am. Bull.* **1989**, *101*, 35–643. [CrossRef]
60. Sun, W.; McDonough, W. Chemical and isotopic systematics of oceanic basalts: Implications for mantle composition and processes. *Geol. Soc. Lond. Spec. Publ.* **1989**, *42*, 313–345. [CrossRef]
61. Yu, J.Y.; Li, X.M.; Wang, G.Q.; Wu, P.; Yan, Q.J. Zircon U-Pb ages of Huitongshan and Zhangfangshan ophiolite in Beishan of Gansu-Inner Mongolia border area and their significance. *Geol. Bull. China* **2012**, *31*, 2038–2045. (In Chinese with English abstract)
62. Yang, S.H.; Miao, L.C.; Zhang, F.C.; Meng, Q.R.; Zhu, M.S.; Munkhtsengel, B.; Chinmedtseren, A. Zircon age and geochemistry of the Tost bimodal volcanic rocks: Constraints on the Early Carboniferous tectonic evolution of the South Mongolia. *J. Asian Earth Sci.* **2016**, *120*, 29–42. [CrossRef]
63. Niu, Y.Z.; Lu, J.C.; Liu, C.Y.; Xu, W.; Shi, J.Z.; Song, B. Geochronology and distribution of the Upper Carboniferous—Lower Permian Ganquan Formation in the Beishan region, northwestern China and its tectonic implication. *Geol. Rev.* **2018**, *64*, 806–827. (In Chinese with English abstract)
64. Zheng, R.G.; Wu, T.R.; Zhang, W.; Meng, Q.P.; Zhang, Z.Y. Geochronology and geochemistry of late Paleozoic magmatic rocks in the Yinwaxia area, Beishan: Implications for rift magmatism in the southern Central Asian Orogenic Belt. *J. Asian Earth Sci.* **2014**, *91*, 39–55. [CrossRef]
65. Xue, S.C.; Li, C.; Qin, K.Z.; Tang, D.M. A non-plume model for the Permian protracted (266–286 Ma) basaltic magmatism in the Beishan–Tianshan region, Xinjiang, Western China. *Lithos* **2016**, *256–257*, 243–249. [CrossRef]
66. Chen, B.; Qin, K.Z.; Tang, D.M.; Mao, Y.J.; Feng, H.Y.; Xue, S.C.; Yao, Z.S. Lithological, chronological and geochemical characteristics of Cihai iron deposit, Eastern Xinjiang: Constraints on genesis of mafic-ultramafic and syenite intrusions and mineralization. *Acta Petrol. Sin.* **2015**, *31*, 2156–2174.
67. Whalen, J.B. Geochemistry of an island–arc plutonic suite: The Uasilau-Yau Yau intrusive complex, New Britain, PNG. *J. Petrol.* **1985**, *26*, 603–632. [CrossRef]
68. Chappell, B.W.; White, A.J.R. I-and S-type granites in the Lachlan fold belt. Earth Environ. *Earth Environ. Sci. Trans. R. Soc. Edinb.* **1992**, *83*, 1–26. [CrossRef]
69. Eby, G.N. The A-type granitoids: A review of their occurrence and chemical characteristics and speculations on their petrogenesis. *Lithos* **1990**, *26*, 115–134. [CrossRef]
70. Whalen, J.B.; Currie, K.L.; Chappell, B.W. A-type granites: Geochemical characteristics, discrimination and petrogenesis. *Contrib. Mineral. Petrol.* **1987**, *95*, 407–419. [CrossRef]
71. Quan, Y.K.; Mu, M.S.; Yang, D.B.; Yan, X.Y.; Wang, A.Q.; Hao, L.R.; Wang, F. Geochronology and in-situ apatite geochemistry of late Paleoproterozoic A-type granites in the Jiao-Liao-Ji Belt, North China Craton: Implications for petrogenesis and tectonic evolution. *Geochemistry* **2023**, 126009. [CrossRef]
72. King, P.L.; White, A.J.R.; Chappell, B.W.; Allen, C.M. Characterization and origin of aluminous A-type granites from the Lachlan Fold Belt, southeastern Australia. *J. Petrol.* **1997**, *3*, 371–391. [CrossRef]
73. Liu, Z.Y.; Yan, D.D.; Zhao, H.; Gong, T.T.; Xiong, F.H. Petrogenesis and Geological implications of Early Paleozoic Gouli granite in East Kunlun: Constraints from U-Pb Geochronology and Petrogeochemistry. *Mineral. Petrol.* **2022**, *42*, 7–19. (In Chinese with English abstract)
74. Wang, Q.; Zhao, Z.H.; Xiong, X.L. The ascertainment of Late-Yanshanian A-type granite in Tongbai-Dabie orogenic belt. *Acta Petrol. Mineral.* **2000**, *19*, 297–306+315. (In Chinese with English abstract)
75. Wu, F.Y.; Liu, X.C.; Ji, W.Q.; Wang, J.M.; Yang, L. Highly fractionated granites: Recognition and research. *Sci. China Earth Sci.* **2017**, *60*, 1201–1219. (In Chinese with English abstract) [CrossRef]
76. Watson, E.B.; Harrison, T.M. Zircon saturation revisited: Temperature and composition effects in a variety of crustal magma types. *Earth Planet. Sci. Lett.* **1983**, *64*, 295–304. [CrossRef]
77. Eby, G.N. Chemical subdivision of the A-type granitoids: Petrogenetic and tectonic implications. *Geology* **1992**, *20*, 641–644. [CrossRef]
78. Turner, S.P.; Foden, J.D.; Morrison, R.S. Derivation of some A-type magmas by fractionation of basaltic magma: An example from the Padthaway Ridge, South Australia. *Lithos* **1992**, *28*, 151–179. [CrossRef]
79. Mushkin, A.; Navon, O.; Halicz, L.; Hartmann, G.; Stein, M. The petrogenesis of A-type magmas from the Amram Massif, southern Israel. *J. Petrol.* **2003**, *44*, 815–832. [CrossRef]
80. Mu, M.S.; Yang, D.B.; Yang, H.T.; Wang, A.Q.; Hao, L.R.; Wang, F. Petrogenesis of late Paleoproterozoic post-collisional magmatism in southern North China Craton: Insights from geochemistry and Nd-Hf isotopic compositions of A-type granites. *Precambrian Res.* **2022**, *383*, 106887. [CrossRef]
81. Chapman, J.B.; Ducea, M.N.; DeCelles, P.G.; Profeta, I. Tracking changes in crustal thickness during orogenic evolution with Sr/Y: An example from the North American Cordillera. *Geology* **2015**, *43*, 919–922. [CrossRef]
82. Zhu, Y.; Lai, S.; Qin, J.; Zhu, R.; Zhao, S.W.; Liu, M.; Zhang, F.Y.; Zhang, Z.Z.; Yang, H. Magma mixing for the genesis of Neoproterozoic Mopanshan granitoids in the western Yangtze Block, South China. *J. Asian Earth Sci.* **2022**, *231*, 105227. [CrossRef]

83. Griffin, W.L.; Wang, X.; Jackson, S.E.; Pearson, N.J.; O'Reilly, S.Y.; Xu, X.S.; Zhou, X.M. Zircon chemistry and magma mixing, SE China: In-situ analysis of Hf isotopes, Tonglu and Pingtan igneous complexes. *Lithos* **2002**, *61*, 237–269. [CrossRef]
84. Wang, E.T.; Zhai, X.W.; Chen, W.F.; Ma, Z.; Wu, L.; Guo, Z.A.; Wang, Y.; Song, G.R.; Wang, J.R. Late Paleozoictec tonics of Southern Central Asian orogenic belt: Evidence from magmatic rocks in the northern Alxa, Northwest China. *Front. Earth Sci.* **2022**, *10*, 1046122. [CrossRef]
85. Hofmann, A.W.; Jochum, K.P.; Seufert, M.; White, W.M. Nb and Pb in oceanic basalts: New constraints on mantle evolution. *Earth Planet. Sci. Lett.* **1986**, *79*, 33–45. [CrossRef]
86. Saunders, A.D.; Storey, M.; Kent, R.W.; Norry, M.J. Consequences of plume lithosphere interactions. *Geol. Soc. Lond. Spec. Publ.* **1992**, *68*, 41–60. [CrossRef]
87. Dong, M.; Lang, X.H.; Deng, Y.L.; Wang, X.H. Geochronology and Geochemistry Implications for Early Eocene Rongma Gabbros in Southern Margin of the Lhasa Terrane, Tibet. *Earth Sci.* **2022**, *47*, 1349–1370.
88. Li, H.; Li, Y.J.; Xu, X.Y.; Yang, G.X.; Wang, Z.P.; Xu, Q.; Wang, L.J. Petrogenesis and tectonic implications of alkali basalts in Kalamaili area, east Junggar, Xinjiang (NW China): Constraints from petrology, geochronology and geochemistry. *Acta Geol. Sin.* **2021**, *95*, 3282–3300.
89. Nowell, G.; Pearson, D.; Bell, D.; Carlson, R.; Smith, C.; Kempton, P.; Noble, S. Hf isotope systematics of kimberlites and their megacrysts: New constraints on their source regions. *J. Petrol.* **2004**, *45*, 1583–1612. [CrossRef]
90. Schmitz, M.D.; Vervoort, J.D.; Bowring, S.A.; Patchett, P.J. Decoupling of the Lu- Hf and Sm-Nd isotope systems during the evolution of granulitic lower crust beneath Southern Africa. *Geology* **2004**, *32*, 405. [CrossRef]
91. Sun, P.; Wang, Q.; Hao, L.L.; Dan, W.; Qu, Q.; Jiang, Z.Q.; Tang, G.J. A mélange contribution to arc magmas recorded by Nd–Hf isotopic decoupling: An example from the southern Qiangtang Block, central Tibet. *J. Asian Earth Sci.* **2021**, *221*, 104931. [CrossRef]
92. Wu, F.Y.; Li, X.H.; Zheng, Y.F.; Gao, S. Lu-Hf isotopic systematics and their application in petrology. *Acta Petrol. Sin.* **2007**, *23*, 185–220.
93. Yu, J.C.; Mo, X.X.; Yu, X.H.; Zhu, D.C.; Li, Y.C.; Huang, X.F. Petrogenesis and geological implications of the Late Triassic potassic-ultrapotassic rocks in Changdu Block, northern segment of the Sanjiang area. *Acta Petrol. Sin.* **2014**, *30*, 3334–3344. (In Chinese with English abstract)
94. Marini, J.C.; Chauvel, C.; Maury, R.C. Hf Isotope Compositions of Northern Luzon Arc Lavas Suggest Involvement of Pelagic Sediments in Their Source. *Contrib. Mineral. Petrol.* **2005**, *149*, 216–232. [CrossRef]
95. Yogodzinski, G.; Vervoort, J.; Brown, S.T.; Gerseny, M. Subduction Controls of Hf and Nd Isotopes in Lavas of the Aleutian Island Arc. *Earth Planet. Sci. Lett.* **2010**, *300*, 226–238. [CrossRef]
96. Liu, X.C.; Chen, B.L.; Jahn, B.M.; Wu, G.G.; Liu, Y.S. Early Paleozoic (ca. 465 Ma) eclogites from Beishan (NW China) and their bearing on the tectonic evolution of the southern Central Asian Orogenic Belt. *J. Asian Earth Sci.* **2010**, *42*, 715–731. [CrossRef]
97. Li, R.W.; Zhang, X.; Shi, Q.; Chen, W.F.; An, Y.; Huang, Y.S.; Liu, Y.X.; Wang, J.R. Geochemistry and Nd–Hf isotopes of the Early Permian volcanic rocks in Hangwula of northern Alxa area and their tectonic significance. *Geol. Bull. China* **2020**, *39*, 647–658. (In Chinese with English abstract)
98. Nielsen, S.G.; Marschall, H.R. Geochemical evidence for me'lange melting in global arcs. *Sci. Adv.* **2017**, *3*, e1602402. [CrossRef]
99. Zhang, G.Z.; Xin, H.T.; Duan, L.F.; Niu, W.C.; Tian, J.; Zhang, Y. Geochemical characteristics and tectonic implications of the end Early Permian high magnesium gabbro from northern Beishan orogenic belt, Inner Mongolia. *Earth Sci.* **2020**, *47*, 3258–3269. (In Chinese with English abstract)
100. McKenzie, D.; O'Nions, R.K. Partial Melt Distribution From Inversion of Rare Earth Element Concentrations. *J. Petrol.* **1991**, *32*, 1021–1091. [CrossRef]
101. Miller, C.F.; McDowell, S.M.; Mapes, R.W. Hot and cold granites? Implications of zircon saturation temperatures and preservation inheritance. *Geology* **2003**, *31*, 529–532. [CrossRef]
102. Schiano, P.; Monzier, M.; Eissen, J.P.; Martin, H.; Koga, K.T. Simple mixing as the major control of the evolution of volcanic suites in the Ecuadorian Andes. *Contrib. Mineral. Petrol.* **2010**, *160*, 297–312. [CrossRef]
103. Zhu, D.C.; Mo, X.X.; Pan, G.T.; Zhao, Z.D.; Dong, G.C.; Shi, Y.R.; Liao, Z.L.; Wang, L.Q.; Zhou, C.Y. Petrogenesis of the Earliest Early Cretaceous Mafic Rocks from the Cona Area of the Eastern Tethyan Himalaya in South Tibet: Interaction between the Incubating Kerguelen Plume and the Eastern Greater India Lithosphere? *Lithos* **2008**, *100*, 147–173. [CrossRef]
104. Xie, F.Q.; Wu, J.H.; Sun, Y.H.; Wang, L.D.; Wu, J.Z.; Jia, W.J. Permian to Triassic tectonic evolution of the Alxa Tectonic Belt, NW China: Constraints from petrogenesis and geochronology of felsic intrusions. *Lithos* **2021**, *384*, 105980. [CrossRef]
105. Rudnick, R.L.; Gao, S. Composition of the Continental Crust. *Treatise Geochem.* **2003**, *3*, 1–64.
106. Condie, K.C. Episodic continental growth models: After thoughts and extensions. *Tectonophysics* **2000**, *322*, 153–162. [CrossRef]
107. Collins, W.J.; Belousova, E.A.; Kemp, A.I.S.; Murphy, J.B. Twocontrasting Phanerozoic orogenic systems revealed by hafnium isotope data. *Nat. Geosci.* **2011**, *4*, 333–337. [CrossRef]
108. Bu, T.; Wang, G.Q.; Huang, B.T.; Dong, Z.C.; Guo, L. Neoproterozoic A-type granites in northern Beishan Orogenic Belt: Early response of the Rodinia supercontinent break-up. *Acta Petrol. Sin.* **2022**, *38*, 2988–3002. [CrossRef]
109. Wang, H.T.; Ren, W.X.; Zhao, Q.X.; Liu, Z.R.; Wang, T.C.; Zhao, H.X. Geochemical Characteristics and Tectonic Significance of A-typeGranite in the South Margin of Zhaobishan, Beishan Area. *Northwest. Geol.* **2016**, *49*, 39–49. (In Chinese with English abstract)

110. Zhang, Y.Y.; Guo, Z.J. Accurate constraint on formation and emplacement age of Hongliuhe ophiolite, boundary region between Xinjiang and Gansu Provinces and its tectonic implications. *Acta Petrol. Sin.* **2008**, *24*, 803–809. (In Chinese with English abstract)
111. Zheng, R.G.; Wang, Y.P.; Zhang, Z.Y.; Zhang, W.; Meng, Q.P.; Wu, T.R. Geochronology and Geochemistry of Yinwaxia Acidic Volcanic Rocks in the Southern Beishan: New Evidence for Permian Continental Rifting. *Geotecton. Metallog.* **2016**, *40*, 1031–1048. (In Chinese with English abstract) [CrossRef]
112. Xia, L.Q.; Xia, Z.C.; Xu, X.Y.; Li, X.M.; Ma, Z.P. The discrimination between continental basalt and island arc basalt based on geochemical method. *Acta Petrol. Mineral.* **2007**, *26*, 77–89. (In Chinese with English abstract)
113. Zuo, G.C.; He, G.Q. *Plate Tectonics and Metallogenic Regularities in Beishan Region*; Peking University Press: Beijing, China, 1990; pp. 1–226. (In Chinese with English abstract)
114. Zhang, D.D.; Wang, J.Q.; Niu, Y.Z.; Zhang, Y.X.; Shi, J.Z.; Liu, Z.L. Provenances of the Lower-Middle Permian in Beishan region, Central Asian Orogenic Belt and its paleo geographic implication. *Acta Geol. Sin.* **2023**, *97*, 307–324.
115. Niu, Y.Z.; Liu, C.Y.; Shi, G.R.; Lu, J.C.; Xu, W.; Shi, J.Z. Unconformity-bounded upper Paleozoic mega sequences in the Beishan region (NW China) and implications for the timing of the Paleo-Asian Ocean closure. *J. Asian Earth Sci.* **2018**, *167*, 11–32. [CrossRef]
116. Pearce, J.A.; Harris, N.B.W.; Tindle, A.G. Trace element discrimination diagrams for the tectonic interpretation of granitic rocks. *J. Petrol.* **1984**, *25*, 956–983. [CrossRef]
117. Pearce, J.A.; Norry, M.J. Petrogenetic implications of Ti, Zr, Y, and Nb variations in volcanic rocks. *Contrib. Mineral. Petrol.* **1979**, *69*, 33–47. [CrossRef]